University of Missouri – Kansas City

Department of Physics & Astronomy
Department of Computer Science & Electrical Engineering
Department of Civil & Mechanical Engineering
Kansas City, MO 64110-2499

30 NOV 2018

Annual Technical Report: UMKC-cUAV-2018-01

ONR Short Pulse Research, Evaluation and non-SWaP Demonstration for C-sUAV Study:

FY2018 ONR HPM Program Annual Report

N00014-17-1-3016 [OSPRES Grant]

by

E.R. Myers, T. Fields, J.A. Crow, D. Chatterjee, P. Rulis, P. Doynov, A. Hassan, J. Lancaster, F. Khan, J. Verzella, J. Beaudin, L. Moler and A.N. Caruso*

University of Missouri – Kansas City, Kansas City, MO

Distribution Statement A: Distribution unlimited.

*Direct all correspondence to:
Anthony N. Caruso, carusoan@umkc.edu, 816-235-2505

Distribution

ADDRESSEE	DODAAD CODE	QUANTITY
Office of Naval Research ATTN: Ryan Hoffman ONR, 351 875 North Randolph St. Arlington, VA 22203-1995	N00014	1
Administrative Contracting Officer* *Transmittal letter only Fax: 312-353-6089	S1403A	1
DEFENSE TECHNICAL INFORMATION CENTER 8725 JOHN J. KINGMAN RD SUITE 0944 FORT BELVOIR, VA 22060-6218 E-mail: TR@dtic.mil	HJ4701	2
DIRECTOR, NAVAL RESEARCH LAB ATTN: CODE 5596 4555 OVERLOOK AVENUE, SW WASHINGTON, D.C. 20375-5320 E-mail: reports@library.nrl.navy.mil	N00173	1

REPORT DOCUMENTATION PAGE	Form Approved OMB No. 0704-0188

The public reporting burden for this collection of information is estimated to average 1 hour per response, including the time for reviewing instructions, searching existing data sources, gathering and maintaining the data needed, and completing and reviewing the collection of information. Send comments regarding this burden estimate or any other aspect of this collection of information, including suggestions for reducing the burden, to Department of Defense, Washington Headquarters Services, Directorate for Information Operations and Reports (0704-0188), 1215 Jefferson Davis Highway, Suite 1204, Arlington, VA 22202-4302. Respondents should be aware that notwithstanding any other provision of law, no person shall be subject to any penalty for failing to comply with a collection of information if it does not display a currently valid OMB control number.
PLEASE DO NOT RETURN YOUR FORM TO THE ABOVE ADDRESS.

1. REPORT DATE *(DD-MM-YYYY)*	2. REPORT TYPE	3. DATES COVERED *(From - To)*
30-11-2018	Annual	SEPT 2017 - SEPT 2018

4. TITLE AND SUBTITLE
ONR Short Pulse Research, Evaluation and non-SWaP Demonstration for C-sUAV Study: FY2018 ONR HPM Program Annual Report

5a. CONTRACT NUMBER
N00014-18-C-1017

5b. GRANT NUMBER
N00014 - 17 - 1 - 3016

5c. PROGRAM ELEMENT NUMBER

6. AUTHOR(S)
E.R. Myers, T. Fields, J.A. Crow, D. Chatterjee, P. Rulis, P. Doynov, A. Hassan, J. Lancaster, J. Verzella, F. Khan, J. Beaudin, L. Moler, and A.N. Caruso

5d. PROJECT NUMBER

5e. TASK NUMBER

5f. WORK UNIT NUMBER

7. PERFORMING ORGANIZATION NAME(S) AND ADDRESS(ES)
University of Missouri - Kansas City
5100 Rockhill Rd
Kansas City, MO 64110

8. PERFORMING ORGANIZATION REPORT NUMBER
UMKC-cUAV-2018-01

9. SPONSORING/MONITORING AGENCY NAME(S) AND ADDRESS(ES)
Office of Naval Research
One Liberty Center, 875 N. Randolph
Arlington, VA. 22203

10. SPONSOR/MONITOR'S ACRONYM(S)
ONR

11. SPONSOR/MONITOR'S REPORT NUMBER(S)

12. DISTRIBUTION/AVAILABILITY STATEMENT
Distribution Statement A. Approved for public release: distribution unlimited.

13. SUPPLEMENTARY NOTES

14. ABSTRACT
This report summarizes the first year's progress of fundamental research in the areas of effects measurement, HPM system development, and RF Coupling with focus on developing a counter UAV system. The contents of this report cover the period from Sept 2017 to Sept 2018 and presents progress made by the researchers listed as authors of the report during the reporting period.

15. SUBJECT TERMS
Microwave, UAV, HPM, Pulsed power, PCSS

16. SECURITY CLASSIFICATION OF:			17. LIMITATION OF ABSTRACT	18. NUMBER OF PAGES	19a. NAME OF RESPONSIBLE PERSON
a. REPORT	b. ABSTRACT	c. THIS PAGE			Anthony Caruso
U	U	U	SAR	59	19b. TELEPHONE NUMBER *(Include area code)* 816-235-2505

Standard Form 298 (Rev. 8/98)
Prescribed by ANSI Std. Z39.18

Additional Distribution: Collaborators/Consultants/Support

Air Force Research Laboratory
ASR Corporation
Atlas Team
BAE Systems – New Hampshire
BAE Systems – Minnesota
Booz Allen Hamilton
Department of Energy's Kansas City National Security Campus, Managed by Honeywell
Eagle Harbor Technologies, Inc.
Georgia Tech Research Institute
KalScott Engineering, Inc.
Lawrence Livermore National Laboratory
Lockheed Martin Missiles and Fire Control
Metamagnetics
Missouri University of Science & Technology
Naval Air Systems Command
Naval Research Laboratory
Naval Surface Warfare Center, Dahlgren Division
Preston Grounds Consulting
Radiation Detection Technologies, Inc.
Raytheon Integrated Defense Systems
Scientific Applications & Research Associates, Inc.
Thomas Hussey
University of Missouri – Columbia
University of Missouri – Kansas City
Verus Research

Table of Contents

1) Photoconductive Switches 12
   A. Fundamental PCSS Development 12
   B. GaN:C Calculations Subgroup 22
2) Small Unmanned Aerial Vehicle Testing and Design of Experiments 25
   A. UAV Diagnostic System Development 25
   B. UAV GTEM Testing 25
   C. Data Analysis and Effects Results 25
   D. Ongoing and Future Research Plan 26
3) Positive Feedback Non-Linear Transmission Lines (NLTL) 26
   A. Major Challenges and Measures Taken 27
   B. Future Plans 30
4) Applied RF Coupling Simulation and Modeling of sUAV 30
   A. sUAV Shapes, Material Compositions, and Electronics Review 31
   B. Characteristic Mode Analysis of UAV frames 33
   C. Experimental Verifications of CMA results 42
   D. Future Work 45
   E. Products, Publications, Patents, License Agreements, etc. 46
   F. References 46
5) Focus Wave Mode (FWM) 48
   A. Introduction 49
   B. Analysis of EM Pulse Propagation 50
   C. Pulsed Excitation 50
   D. Time Harmonic Excitation 52
   E. Time-Harmonic Bessel Beams 52
   F. Results and Discussions 53
   G. Future Investigation 57
   H. Summary and Conclusions 57
   I. References 57
Appendix 59

Acknowledgements

The C-sUAV team would like to thank Jeffrey Newhook, James Verzella, and Steve Siegel from the UMKC fabrication shop for design and manufacture of multiple parts to support testing, Si-PCSS thermal mitigation, and equipment repair. James Verzella, has also provided assistance in testing and providing technical written material for the monthly status reports. Thanks to Jake Walker from NSWC Dahlgren for approving the NIRF amps as government furnished equipment.

We would also like to thank Steve Bellinger (RDT), John McGeehan and Yannick Morel (BAE NH), Sean Ahern and Mike Hatfield (BAH), Randy Curry (MU), Karl Hobart, Fritz Kub, Andy Koehler and Travis Anderson (NRL), John Tatum (SURVICE), Tom Hussey, Lee Jackson and Chip Grounds (ONR), Ben Grady, Matt McQuage, Bill Camp and Cory Hoshor (NSWCDD), Adam Conway and Lars Voss (LLNL), Robert Koslover, John Krill and Jonathan Parsons (SARA), who have all gone above and beyond to provide suggestions and recommendations along the way outside of their normal duties.

Lastly, a big thank you to Heather Little and Leta Moler for all security and administrative support, without which, the program would not function.

Acronyms

CFD - Computational Fluid Dynamics

cUAV – Counter Unmanned Aerial Vehicle

DoE – Design of Experiments

EL – Electroluminescence

GaN – Gallium Nitride

GTEM – Gigahertz Transverse Electro-Magnetic

HPM – High Power Microwave

NLTL – Non-linear Transmission Line

OSPRES - ONR Short Pulse Research, Evaluation, and non-SWaP

PCSS – Photoconductive Solid-State Switch

RDT – Radiation Detection Technologies

RF – Radio Frequency

TCAD – Technology Computer Aided Design

UAV – Unmanned Aerial Vehicle

OSPRES Program Description

The objective of the OSPRES program is to map small unmanned aerial vehicle (sUAV) effects space, empirically and by simulation, as a function of high power microwave (HPM) waveform (power density, frequency, bandwidth, pulse repetition frequency, angle-of-incidence, polarization, pulse shape and pulse width). Then, use the waveform space(s) that enable control over the desired levels-of-lethality on sUAV and similar targets, with the least power density, to drive development of transitionable HPM sources and electronically steerable radiators. Effects measurement, HPM system development, and RF Coupling through simulation are the three signature areas of the program.

The overall OSPRES program is broken by grant (N00014-17-1-3016) and contract (N00014-18-C-1017) execution vehicles. The formal name of the grant is the *ONR Short Pulse Research, Evaluation and non-SWaP Demonstration for C-sUAV Study*. The contract is named the *ONR Short Pulse Research, Evaluation and non-SWaP Demonstration for C-sUAV*. Annual reports for the grant and contract will be available on DTIC in DEC and MAY, respectively. This report covers the grant execution during the period, SEPT2017 – SEPT2018, and is comprised of results from the UMKC faculty and staff scientists. Following the executive summary is a technical summary of each thrust area. Following the thrust area descriptions are copies of all monthly reports for the grant. The purpose of splitting the work between grant and contract was/is to separate out the more fundamental from applied efforts, which could be more openly disseminated.

Year 1 - Executive Summary

The OSPRES (ONR Short Pulse Research, Evaluation and non-SWaP) program performed fundamental work in the areas of Silicon (Si) and Gallium Nitride (GaN) based photoconductive switch development, measurement of HPM waveform dependent effects on small unmanned aerial vehicle (sUAV), adaptive design of experiments, noise injection, RF coupling to sUAV's, minimally dispersive wave theory, and positive feedback non-linear transmission line (NLTL) development. The report that follows summarizes the progress made in each of the above sub-areas during Year 1. Some of the most notable achievements are listed in Figure ES1.

The photoconductive solid state switch (PCSS) subgroup continuously worked to develop a fundamental understanding of the limitations of Silicon and Gallium Nitride based photoconductive switches and their application to pulsed power, in light of historical achievements in the field. With an estimated 2 megawatts (MW) peak power generation (benchtop equivalent), the Si-PCSS subgroup has succeeded in achieving one-third of the peak power required for an individual element in the envisioned phased array required to meet the mission needs. Si-PCSS's have been integrated with a rapid charge capacitor system and pulse forming transmission lines for pulse testing. Si-PCSS hold-off voltage has been pushed to >6-kV with 3-kV output pulse moving closer to the project goal of 10-kV hold-off. Currently, thermal mitigation issues are the primary issue plaguing the Si-PCSS group. Cooling system designs are changing weekly and progressively moving towards a goal of 500-W/cm^2 cooling capacity.

UMKC's effects team has, over the last year, developed a custom UAV model for RF effects testing, written code for the automation of testing, and researched the areas of an adaptive design of experiments (DoE) and noise injection. The adaptive DoE was developed to refine/inform optimum source parameters that will result in known effects on sUAV's and further inform the requirements for a tunable HPM system with control over the policy desired levels-of-lethality. The effects team has also traveled to multiple test locations over the last four months performing over 1300 effects tests with the custom UAV and are beginning to analyze data for trends in source parameters and sUAV effects. The adaptive DoE and noise injection projects are discussed within this report, the effects analysis/trends are presented in the contract portion of the reports/program.

UMKC's GaN:C simulations/modeling subgroup has made progress in optimizing GaN:C for a high power, high repetition rate solid state switch. During year 1, they have computed electronic structure properties of GaN:C including the optical and symmetric band structure of GaN:C. They have obtained the software to perform GaN-PCSS device level calculations to model optical absorption, hold-off voltage, and thermal dissipation relevant to determining the optimum design of a GaN:C based PCSS.

The RF coupling subgroup has used Characteristic Mode Analysis (CMA) to computationally quantify electromagnetic coupling and interference to UAV frames over the L-band and S-band and validated CMA coupling predictions using experimental measurements. Also the RF coupling group has reviewed the most common sUAV shapes, sizes, material compositions, and electronics commercially available and developed a table of occurrences and frequency in sUAV's.

The Positive Feedback NLTL group has developed a positive feedback power amplifier coupled with a nonlinear transmission line generating ones-of-kW power RF pulses in a closed-loop network coupled with a 9-section 1200 V rated schottky diode NLTL. They have performed several closed-loop experiments at low voltage level within a frequency range of 5 to 70-MHz and achieved continuous RF signal outputs with positive gain at different stages of the NLTL.

Preliminary results of the Focused Wave Mode (FWM) group suggest that EM pulses with smaller rise times can effectively launch electromagnetic waves whose time-average power density shows minimal spatial decay contrary to the standard $1/r^2$ decay of EM waves. They designed and simulated low-profile, ultra-wideband micro-strip patch antennas to demonstrate the potential of launching low dispersion EM waves with results demonstrating the feasibility of short EM pulses for c-sUAV ranges relevant to the project.

Also, the UMKC HPM group has stood up a research facility with its own Gigahertz TEM (GTEM) testing platform. Reconstruction and security issues have been integrated, facilitating source and effects testing in a secure environment. With the GTEM, Si-PCSS based HPM testing will transition from benchtop testing to a controlled environment with sUAV targets.

***Figure ES1**. Notable achievements and progress of OSPRES program by quarter.*

Annual Report – Technical Areas Research Summary

1) Photoconductive Switches

A. Fundamental PCSS Development

Overview

The fundamental photoconductive solid-state switch (PCSS) development subgroup has focused primarily on optimization of the Si-PCSS hold-off voltage, on-state resistance (R_{on}), and recovery time. The effort on these three areas has been dedicated to developing a better understanding of the underlying physics governing the metrics, and collecting the experimental data necessary to improve upon them. Figure 1 provides a summary timeline of our progress over the reporting year.

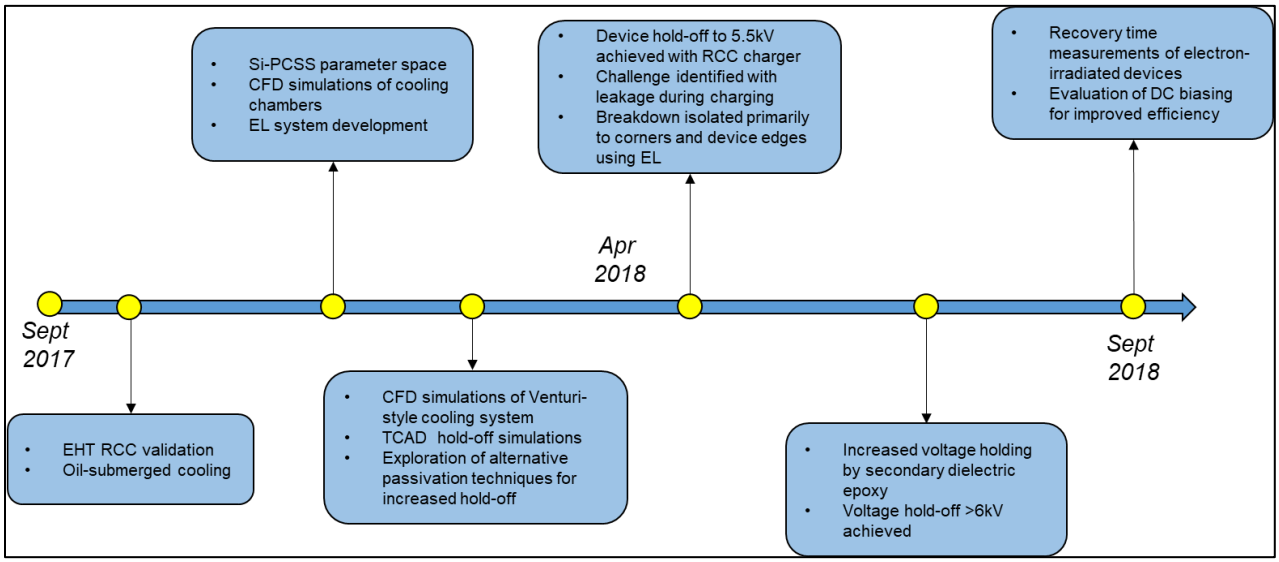

Figure 1. *Summary timeline of fundamental Si-PCSS development from September 2017 through September 2018.*

Initial efforts from UMKC on fundamental Si-PCSS development centered on mapping the available device parameter space for optimization. Considered parameters were broken into two major categories: (1) device design (passivation, doping profiles, contacts, geometry) and (2) optical coupling (wavelength, coherence, pulse width, angle of incidence, anti-reflective coatings, and incidence profile). Considering the state of the technology and the ability of our team to execute on characterizing device parameters, we concluded that hold-off voltage, on-state resistance (R_{on}), and recovery time were the most critical performance metrics and accordingly prioritized improving passivation, doping profiles, and device geometry in addition to modeling R_{on} and carrier recombination.

Simulation and Modeling

The simulation and modeling effort focused on improving the Si-PCSS design for increased hold-off voltage and opto-electrical modeling of static and transient behavior of the devices. Successes in these areas have been modest as team members develop the foundations in simulation and modeling of photoconductive switches.

Hold-off Voltage

A large number of TCAD simulations were conducted exploring various device parameters that control hold-off voltage. These parameters included device thickness, doping profile and junction depth, edge beveling, and metal contact geometry. Conclusions from these simulations are to be interpreted as relative changes in hold-off voltage, rather than absolute due to challenges in accurate modeling of surface effects such as dangling bonds, inversion layers, and surface topology. Despite these limitations, we believe the following conclusions can be made from simulations of Si-PCSS device breakdown voltage: (1) increasing device thickness increases hold-off voltage, (2) decreasing the doping profile gradient increases device-hold off voltage, (3) edge-beveling at the optimal angle reduces peak electric fields at the junction surface, and (4) extending the soldered contacts over the edge of the device improved device hold-off.

The simulations conducted on device thickness and extending the doping profile served as a litmus test to confirm our expectations. However, the results for both of these were surprisingly more extreme than expected. For example, a 200-µm increase in thickness resulted in nearly a 3-kV increase in breakdown voltage. Similarly, when comparing square, Gaussian, and exponential doping profiles, a 500-V and 1-kV increase in hold-off resulted from the exponential profile when compared to the Gaussian and square profiles, respectively.

Regarding edge-beveling simulations, the resulting hold-off voltage was virtually negligible, although there was a clear reduction in peak electric field at the junction surface. The lack of an associated increase in hold-off is believed to be due to limitations of TCAD in accurately simulating surface phenomena. This will soon be confirmed experimentally, as Radiation Detection Technologies (RDT) has recently delivered devices with a 45° bevel for experimental evaluation.

Extending the contacts over the edge of the device was perhaps the most surprising result from simulation, indicating that a simple change in packaging improves the hold-off voltage by moving the peak electric field points away from the device junction where it may be mitigated via dielectric encapsulation, per Figure 2. This also confirmed the recent success in hold-off voltages with devices with extended contacts, between which was filled with a second passivating epoxy.

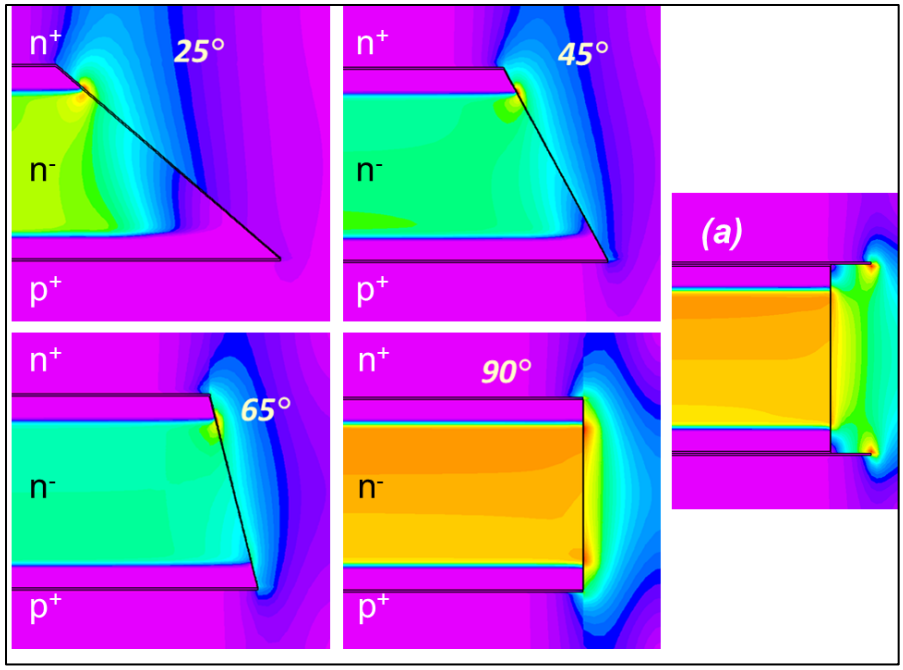

Figure 2. *TCAD simulations of edge beveling at 25°,45°,65°,90° and (a) 90° with the contacts extending the contacts over the device edge., and (b) 90° with contact extension.*

Opto-electrical Modeling

The opto-electrical modeling effort began with an analytical model of the photo-carrier generation as a function of incident light in order to better understand the laser requirements for the Si-PCSS system and the effects of free carrier absorption on R_{on}. The free carrier absorption only contributed to the transmittance of light through the heavily doped N-type region (device window). At doping concentrations above approximately 5×10^{19} cm^{-3}, free carrier absorption resulted in less than 30% of the light entering the intrinsic region. Alternatively, below concentrations of 1×10^{19} cm^{-3}, 70% of the incident light makes it through to the intrinsic region.

However, the modeling conducted so far is limited in its ability to accurately represent the R_{on} of the Si-PCSS system during pulse testing because it does not incorporate any transient carrier drift or diffusion. In effect, we are able to calculate changes in on-state resistance, but not absolute.

Over the coming months, UMKC will emphasize transient modeling of the Si-PCSS devices by first incorporating drift and diffusion into the model, followed by simulation of the pulse forming networks used during device testing.

Device Characterization

Breakdown Characterization

The Si-PCSS hold-off voltage has been improved by nearly six-fold (to over 6 kV) over the course of year one. The improvement was achieved in two ways: (1) by reducing the

duration of the high-voltage via the Eagle Harbor Technologies Rapid Capacitor Charging System (RCC), and (2), by the use of two-layer passivation using a junction-grade polyimide combined with a dielectric epoxy, informed in part by electroluminescence studies at UMKC.

To better understand the causes and mechanisms of device breakdown, UMKC designed and built an electroluminescence system to conduct reverse bias electroluminescence (ReBEL). The system was programmed in LabVIEW using a general purpose data acquisition system from LabJack, high voltage power supplies, and an Apogee F8300 camera. A photo of the final system is shown in Figure 3.

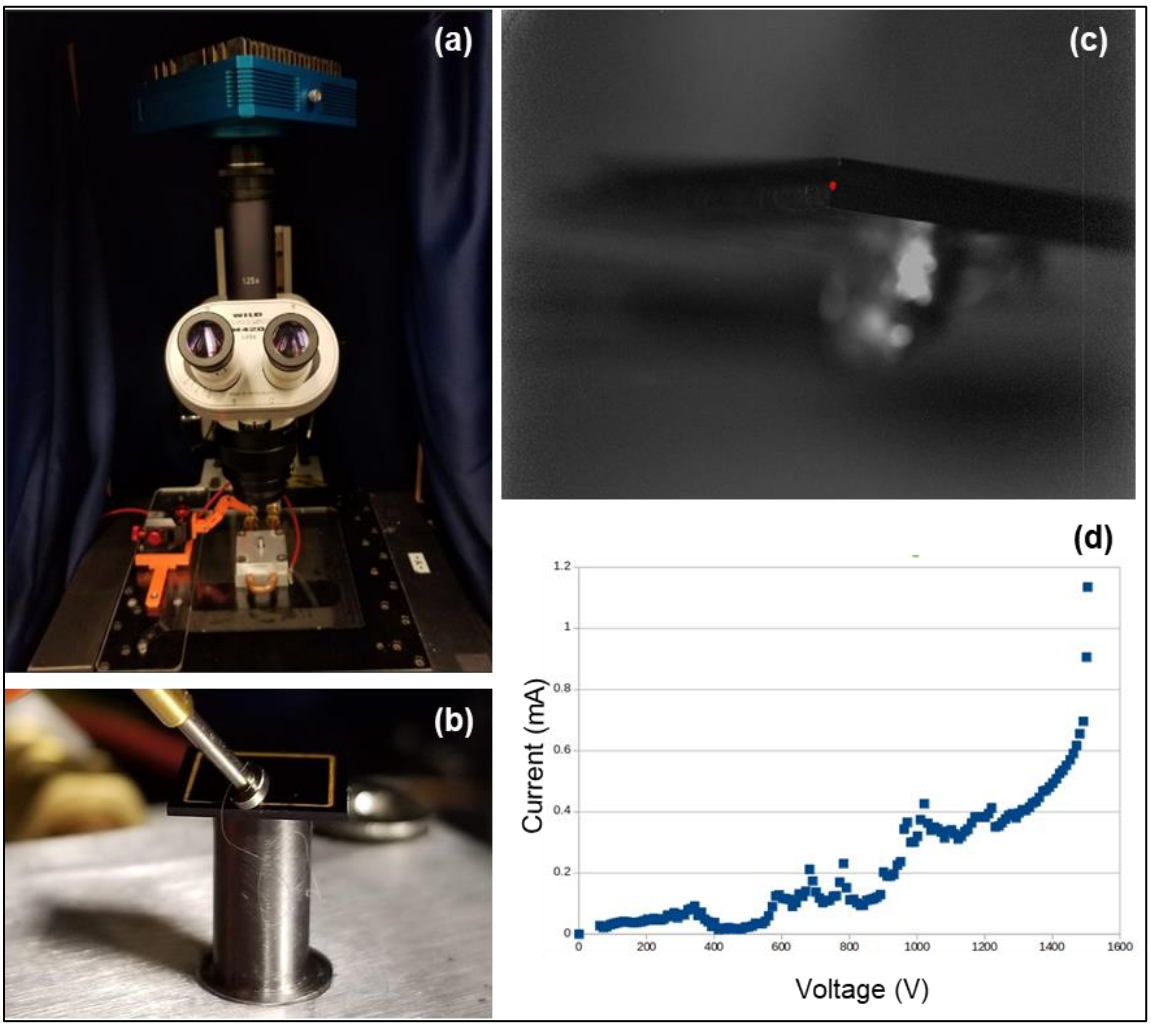

Figure 3. *Electroluminesence system developed at UMKC for avalanche breakdown evaluation: (a) photo of electrolumenesence system from user perspective, (b) photo of Si-PCSS under test. (c) electroluminesence image overlay of breakdown occuring on corner edge of Si-PCSS, as indicated in red, and (d) Si-PCSS IV curve during ReBEL test.*

Results of the electroluminescence studies on various Si-PCSS devices indicated that the passivation failure occurred primarily at the corners and edges of the Si-PCSS devices. To overcome this limitation, RDT improved their passivation material, application

process, and added a secondary dielectric coating using a high dielectric strength epoxy. The result of these efforts are shown in Figure 4, during which a Si-PCSS device was pulsed at a voltage increments of approximately 100 V, until failure was detected at 5.6 kV. Future efforts to further enhance hold-off voltage include evaluation of beveled devices and additional passivation materials including SIPOS. RDT has recently fabricated 7-cm wide devices with a beveled edge which will be evaluated and reported on during year two.

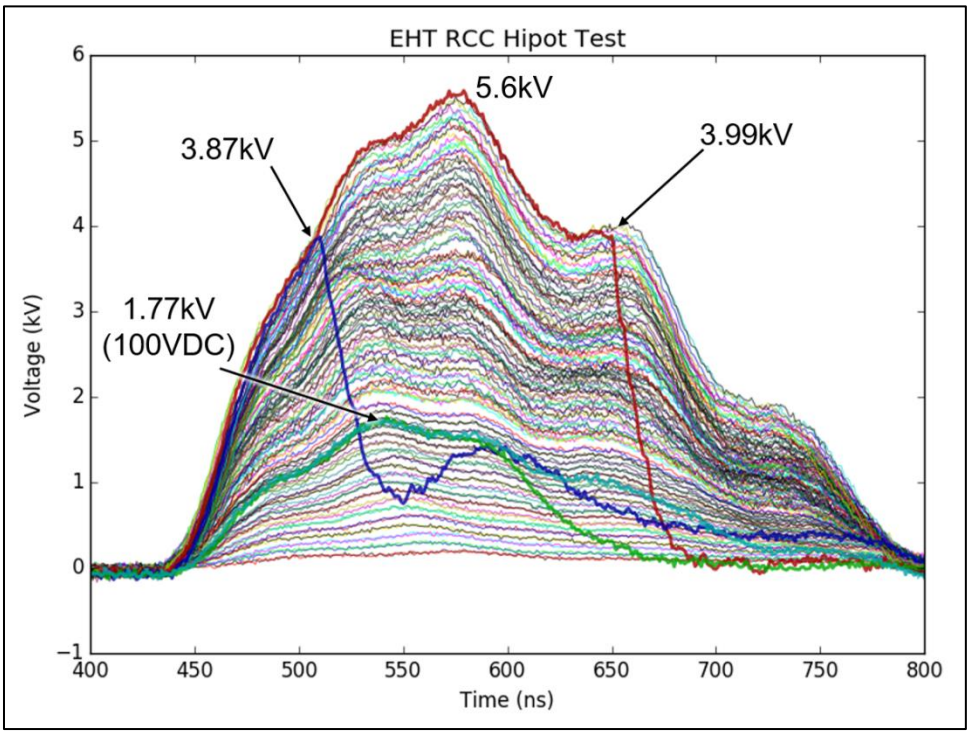

Figure 4. *High voltage breakdown test (hi-pot) using the EHT RCC for short duration hold-off (~200ns FWHM). Si-PCSS system was tested in approximately 100-V increments up to a voltage of 5.6 kV before breakdown was detected. The 5.6-kV test was repeated resulting in breakdown at 3.87 kV during the pulse rise. Subsequent tests were conducted at 1.77 kV during which breakdown was not detected.*

Recovery Time

During early testing, the Si-PCSSs were limited to continuous operation at a charge voltage of a few hundred volts. This was believed to be primarily due to DC charging combined with long recovery times leading to excessive heating immediately after switching. This occurred when the DC charger, including its internal charge storage, immediately began recharging the transmission line, resulting in a large leakage current due to still-present charge carriers.

The RCC was expected to overcome this limitation by pulse charging the transmission line after the switch had recovered, but before the subsequent laser pulse. However, upon evaluation of pulse-charging, we determined that the long recombination of carriers in silicon still caused substantial heating, but the leakage period had shifted to just prior to

switching while the RCC recharged the transmission line. It's important to note that the switch resistance must increase by at least 4-5 orders of magnitude to effectively block charge voltages of 1kV or more. This requires that the number of free carriers decrease by approximately the same order of magnitude.

Alternative charging approaches using a DC supply with added supply resistance on the input of the transmission line were also evaluated. During these tests it became clear that the added resistance resulted in a current limited recharge period and a nearly constant bias voltage until the switch resistance exceeded the series resistance. In effect, control of the supply resistance enabled crude control of the sweep-out rate and—to a lesser extent—the recombination rate.

This effect can be seen in Figure 5, where DC charging data was collected at various energy per pulse (represented by % AOM). As the incident laser energy increased, the total recovery time increased with a constant supply resistance (switch is fully recovered when V_{load} reaches approximately 0 V). The same effect is achieved by reducing supply resistance and holding the incident light constant.

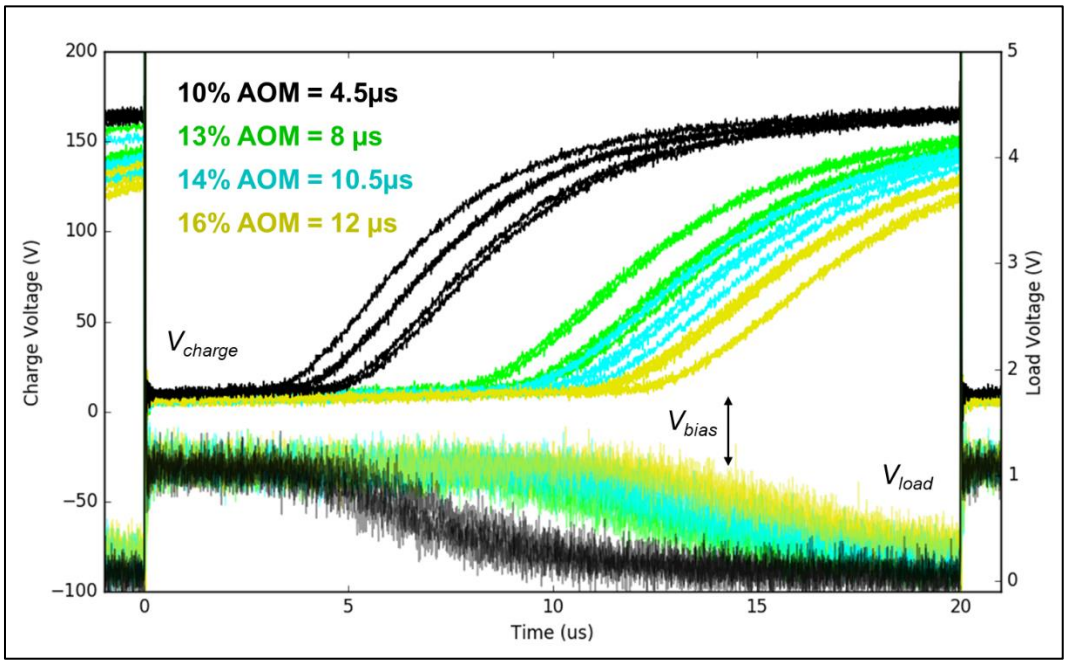

Figure 5. *Charge and pulse voltage waveforms using a DC power supply with additional supply resistance. Tests were conducted at various AOM settings corresponding to incident laser energy per pulse.*

Recent efforts have focused on characterizing the effect of DC bias on recovery time (i.e. carrier sweep-out and recombination time), and the improvements in recovery time achieved via electron-beam irradiation. Devices were received from RDT and evaluated using a reverse bias recovery test before and after electron-beam irradiation at 2-10MR. The absolute and relative change in reverse recovery time is shown in Figure 6.

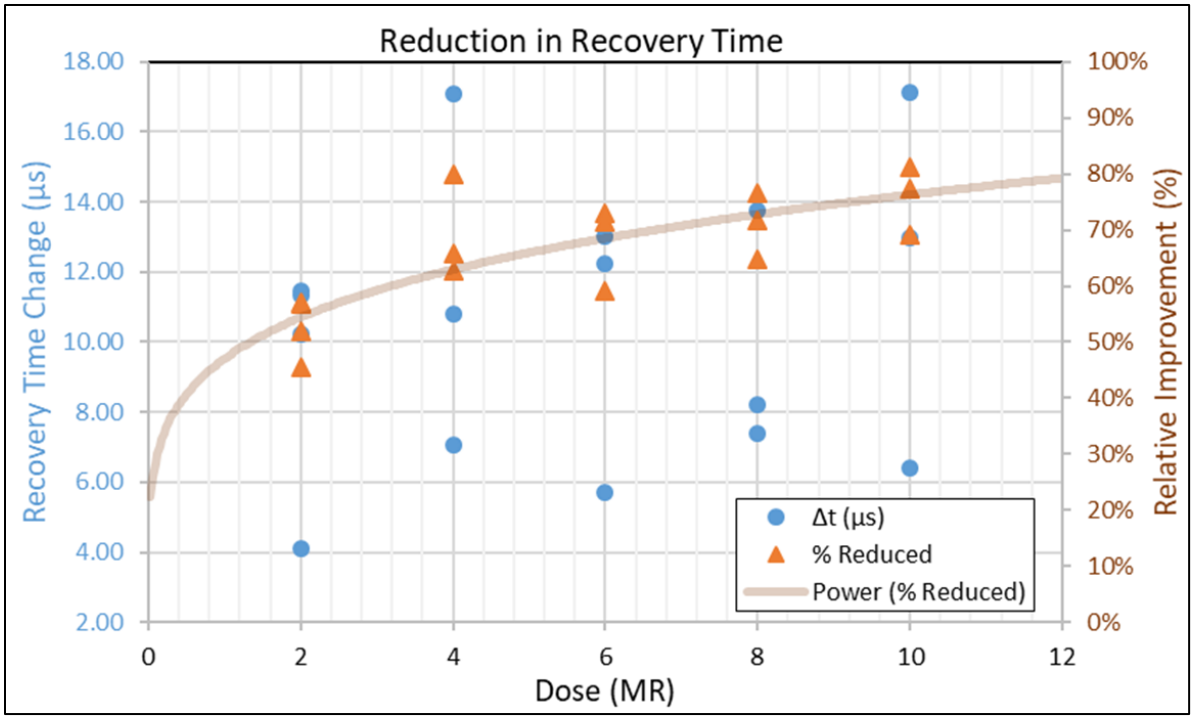

***Figure 6**. Absolute and relative change in recovery time as a function of total radiation dose in mega-Rad on various Si-PCSS devices.*

A 50% reduction in recovery time was achieved at the minimum dose evaluated (2 MRad), indicating a dose below this value may provide the sufficient decrease in recovery time without sacrifices to hold-off voltage. UMKC is currently conducting experiments to evaluate the effect of irradiation on hold-off voltage and R_{on}. The reduction in recovery time may be the most significant improvement in device design. However, these results are very preliminary and will be confirmed in subsequent reports.

GaN:C Device Characterization

With fluctuations in personnel, project management, and with GaN:C being a lesser understood material for pulsed power applications, research has not progressed as far as anticipated in the first year. As such, most of the work on GaN PCSS's has been focused on identifying the optimum laser wavelength for the operation of GaN based PCSS devices. Device heating, pulse pileup, and hold-off voltage are all dependent on the wavelength of the triggering laser. Low voltage variable wavelength photoconductivity and variable wavelength pulse testing has been performed with mixed success on PCSS devices of varying geometry, mounting, and carbon dopant concentration. A summary of successes and failures is presented below.

<u>Low Voltage DC photoconductivity</u>

Early testing with GaN:C devices included low voltage (<500V) DC photoconductivity testing. This test identified the amount of current passing through the GaN switches in the steady state (non-pulsed) as a function of wavelength (Figure 7). It was determined that,

at all voltages, the peak current is obtained with incident light at ~360nm. Results of the DC photoconductivity work informed the ideal wavelength ranges for pulse testing and the variable wavelength pulse testing as the low voltage DC photoconductivity provides no information about carrier generations, device heating, or pulse pileup. This information is left to be determined from pulse testing.

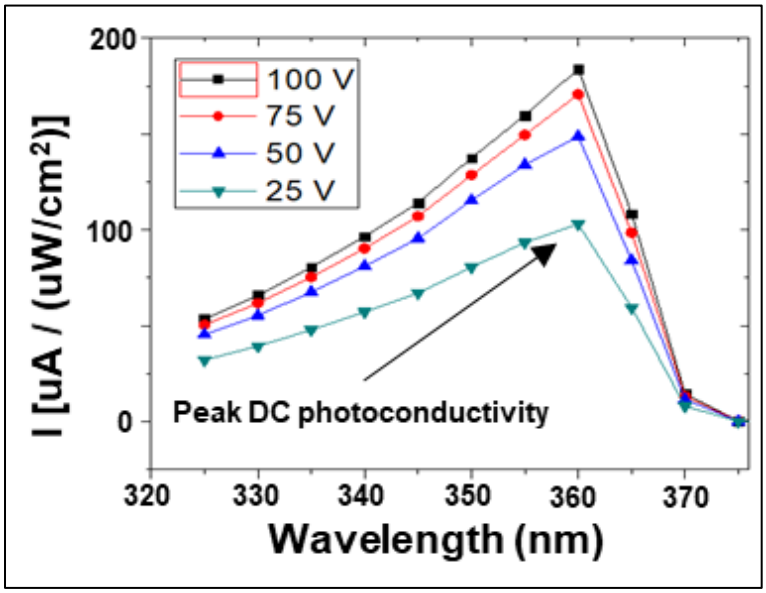

Figure 7. *Photoconductivity of GaN as a function of wavelength. Peak photoconductivity is observed near the bandgap.*

Pulse Testing with 337nm Nitrogen laser

The bulk of GaN device testing during the first year was performed using a 337nm nitrogen laser sourced from a finished research project at UMKC. The laser in question had a suitable wavelength, pulse duration, and power, for pulse testing of GaN PCSS devices. Although the optimum wavelength has not been identified, the nitrogen laser has been useful for preliminary testing and device characterization. Beam shape of the N2 laser is not the ideal Gaussian beam profile usually passed to standard optics for beam steering and focusing. Careful use of beam shaping optics allowed for a more uniform beam profile to be focused on the samples.

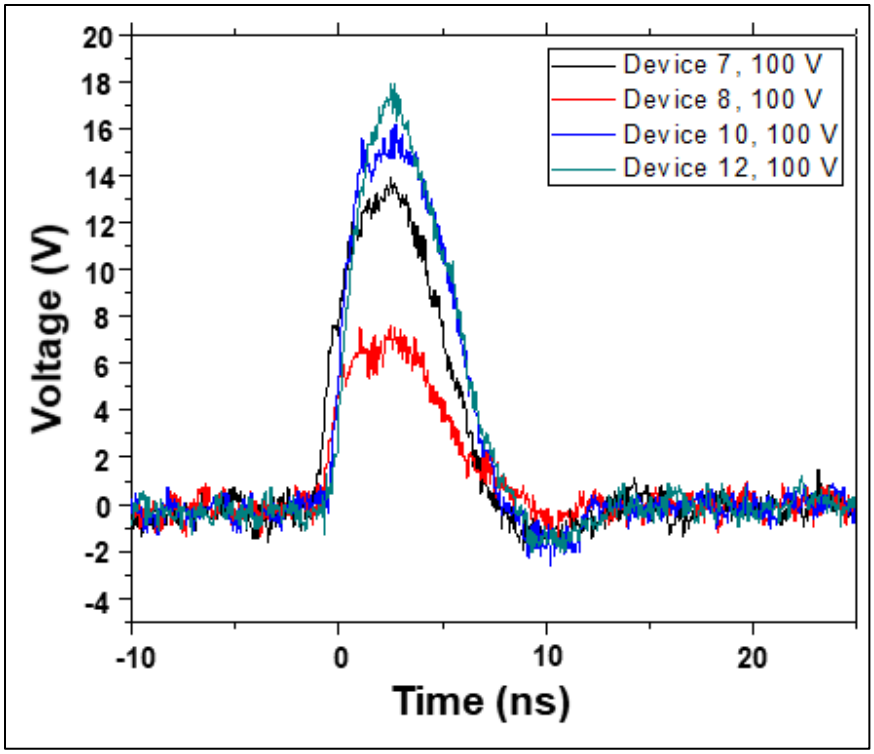

Figure 8. *Pulse testing on GaN PCSS devices with varying contact dimensions and gap width. Device geometry plays a crucial role in on-state resistance and pulse formation.*

Pulse testing on devices with varying contact dimensions and gap width has shown that on-state resistance is highly dependent on the geometry of the device itself (Figure 8). We have also performed testing on a few devices with two different carbon dopant concentrations and have identified that, of the two concentrations, the devices with increased dopant concentration results in increased pulse voltage. Further pulse testing remains to be performed.

Variable Wavelength Pulse Testing

In an effort to identify the optimum wavelength for operating GaN PCSS devices, a variable wavelength pulsed laser was obtained on loan from Opotek Incorporated. The laser was an Opolette 355nm capable of providing ~5ns laser pulses between 220nm to 2100nm. Although the pulse width was too large to effectively operate the GaN PCSS devices for high power pulsed applications, we decided to move forward and see what research questions the laser may have been useful for answering. Over the course of one week, a handful of GaN devices with varying contact length and gap width were pulse tested. Unfortunately, the nuances of working with the laser were a setback and pulse testing did not provide the answers we were looking to obtain. Two of the biggest factors affecting the quality of testing were laser light leakage and output power. The manufacturer failed to disclose the existence of some 532nm and 1064nm laser light leakage in the 340nm – 380nm range identified as the most optimal for GaN. This resulted in multiple wavelengths incident on the devices and it was decided that the situation was not ideal and the data needed to be recollected for proper reporting. To resolve this issue,

we have requested another loaner laser that is expected to be delivered in December with the appropriate filters for removing the unwanted laser lines.

The other factor affecting testing of GaN devices was the output power of the laser. Incident laser power on the devices was quite high below 360nm resulting in device saturation. Before we had the time to analyze the data and determine the devices were in saturation, the laser was due to be returned to the manufacturer. This prevented any reliable data to be obtained from the testing. We have sourced filters to reduce incident laser power for testing with the return of the loaner laser in December.

Other GaN PCSS Research

Other testing performed on GaN devices were 1) capacitive plate testing, 2) mounting configuration, and 3) second and third harmonic pulse testing from a 1064nm laser. The capacitive plate testing was used to explore alternative source voltage for PCSS applications. Testing has so far been inconclusive and was deprioritized while we investigate the optimum wavelength for GaN operation.

The contacts of GaN devices are of small dimension and have presented some difficulty in providing consistent contact and mounting. As a result, analyses for on-state resistance has not been 100% reliable. UMKC currently has three mounting methods for the devices 1) standard soldering, 2) a custom mounting fixture designed and fabricated by NRL, and 3) a PCB based mount designed by LLNL for use with other devices and repurposed for GaN testing. We continue to experiment with all 3 methods to determine which provides the most consistent results while minimizing contributions to on-state resistance.

Most recently, we have started testing with the second and third harmonic laser lines from a 1064nm seed laser with ~70ps pulse width. By purchasing non-linear harmonic generators, we have converted the 1064nm laser in to the second harmonic 532nm and the third harmonic 355nm laser lines. At 355nm, the incident laser light is just below the peak observed in DC photoconductivity. This work is just beginning and results will start to be available in future monthly reports.

Team Management

Reporting on the technical effort of this program in absence of the programmatic and managerial challenges encountered does not accurately represent the successes and failures of the UMKC PCSS team during the reporting year. This section has been included to provide transparency and to clarify the challenges faced and progress made to ensure success in the coming months.

In addition to technical development of the PCSS systems, UMKC spent substantial effort on team building and developing the foundational skillsets of team members to execute on future work. In December 2017, the PCSS-focused team consisted of one staff member, one graduate student, and two undergraduate students. Since that time, a total of nine team members have been added, including two staff, two graduate students, and

five undergraduate students. In addition, the scope of the PCSS team has expanded, incorporating additional members to focus on RF engineering projects for integration and validation of transmission line transformations and measurement necessary for general PCSS integration. Although critical for long-term program execution, the over three-fold increase in team members has dramatically increased organizational demands. Moreover, executing on a *living* program in which the course evolves as new information becomes available has required finding a balance between clear communications of responsibilities and providing a flexible organizational structure. This not only places increased demands on leadership, but on all students to understand their role in the context of the larger program.

The challenge is rooted in balancing the effort needed to execute on specific technical projects while maintaining a fertile environment for scientific and personal development of a student-based team. At times, critical efforts to execute on the technical program have taken priority over maintaining organized communication, while at other times the opposite was true, effort to maintain order trumped progression on specific technical objectives. In part, this is due to the nature of the University environment which is particularly front-loaded (i.e., most demanding early in a program when learning is at the forefront of the research process). To compensate, the UMKC team is currently overhauling its organizational structure by selecting team leaders, re-distributing responsibilities, and establishing processes upon which to lean. We believe the changes being made will only improve future program success.

B. GaN:C Calculations Subgroup

What follows is a summarization of the starting point and accomplishments of the GaN:C theory and simulation subgroup over the past year. The starting point for the GaN:C theory and simulation subgroup was that the high-level goals of the PCSS theory, development, and optimization aspect of the overall project were understood. That is, the goal was to use theory and modeling to help guide the development and optimization of a material (likely GaN:C, but possibly others) to serve as the key device component for a high power, high repetition rate solid state switch. The macroscopic parameters that needed optimization were the magnitude of the electric field hold-off, the photo-absorption cross-section (and effective depth of penetration) in relevant wavelengths, and the rate of thermal energy dissipation.

At the beginning of the project, the GaN:C subgroup consisted of an investigator and a student who were specialists in the conduct of *ab initio* electronic structure calculations and in the atomic scale modeling of systems that required on the order of 100 to 2000 atoms to model the physically relevant phenomena. Although not recognized initially, the first major challenge was simply getting a handle on the range of time and length-scale phenomena that would need to be accounted for in the optimization process. Clearly, the macroscopic properties to be optimized were dependent on the fundamental electronic and atomic structure of the target material. What was not understood at the outset and what needed to be determined over time (and continues to be under study) is *precisely* what atomic and electronic structure properties had macroscale relevance and how those

properties could be cleanly connected to any macroscale simulation. A huge range of possibilities were present, many of which could be extremely challenging to explore individually. Starting with expertise at near to the bottom level of the time and length scale for multi-scale modeling is helpful in that it is an essential foundation, but a deficiency is that the scope of the direction to study is exceptionally large.

Although in principle any material property can be computed from *ab initio* computation, in practice the set of material properties that are accessible are limited. Two key considerations come in to play and it is only when both conditions are met that a computation can actually be performed. If a property of interest depends on highly detailed physics (e.g. requiring a fully relativistic treatment and sophisticated many-body effects) then only a few packages are capable of performing those calculations. For some given property, the number of atoms needed to model that property may be prohibitive for all known algorithms. Only a few packages may be capable of managing large-scale calculations for electronic structure. As an example of the potential complexity, if a property (such as electrical conductivity in the presence of an external electric field) of an otherwise simple crystal such as GaN also required knowledge of how the electronic structure behaves at a GaN:C/AlN interface, a GaN:C grain boundary, or a GaN:Si surface, then some understanding of the atomic structure at those extended defect structures is needed. The number and variety of such structures is very large and determining realistic atomic structures is a significant challenge in itself. The combination of sophisticated physics and structures that require large numbers of atoms is the root of the challenge.

The accomplishments over the past year can be broken down into literature review and educational activities, calculations of electronic structure, and technical computer aided design (TCAD) simulations. Because the specific properties to be optimized are macroscale, but of atomistic and electronic origin, a connection between electronic structure and microscale properties needs to be made. This is a well-known Grand Challenge in materials science because it necessarily connects extremely large time and length scales. Bridging requires connecting equally disparate theories and simulation technologies. Given the expertise of the group, it was a significant but worthwhile challenge to step outside of the realm of atomic scale modeling and electronic structure calculation methods. Group members searched for and read a large number of relevant papers and also searched for and weighed options about what software to invest time and energy into learning.

Simultaneously with the literature review, the electronic structure properties of a range of GaN:C models were computed. Important foundational compute parameters for desired accuracy levels were determined including the number of k-points and supercell sizes. Models of GaN:C were made and relaxed with the C atom in different positions and a range of different electronic structure properties were computed. The symmetric band structures and optical (dielectric function) properties were computed. The C atom defect band energies and influences on the optical spectrum were observed. Quantities such as the band gap at different wave vectors have been noted and will be used in upcoming FLOOXS calculations. Once FLOOXS calculations are in regular production, then we will

likely return to the electronic structure calculations that have already been completed and we will extend them to include the influence of more complicated structures (e.g. interfaces, surfaces, C-atom clustering, etc.). The XANES spectra of the models was computed, which could potentially serve as a point of evidence for later determination of the precise distribution of C dopant atoms. It is possible that experimental measurement of the C-1s XANES spectrum for GaN:C samples would produce a spectrum with a fingerprint structure. Relating the computed spectra to the observed spectra could definitively identify the statistical distribution of C atoms into available positions. That information may be important if the root cause of hold-off limitations is dependent on the C atom site preference. For example, if the break-down occurs in a cascade-mode and the electron phonon coupling matrix elements for certain C sites vs. other sites tends to promote the break-down then efforts to drive the doping process to avoid C occupation at those sites would lead to an improved hold-off field magnitude. The computational side of that avenue for research is currently completed unless and until a need for further spectra is noted.

In regard to TCAD simulations, there are a very wide range of macroscale device simulation tools. Many are commercially available (but exorbitantly expensive) and were it not for the price, they might be appropriate tools for device level analysis. Considerable effort was spent to evaluate the available tools and to identify what path to pursue to be able to compute the desired device level properties (optical absorption, hold-off field magnitude, and thermal dissipation). Presently, the academic software FLOOXS was seen to be the most cost-effective option. This software was acquired and installed in a basic (desktop) environment. The program code has been tested and demonstration level simulation decks have been run. Considerable effort has been spent to prepare FLOOXS for running in a production level environment through the use of the Singularity virtualization software. That effort is ongoing, but nearing completion.

The main list of activities to be pursued in the upcoming year follow. First, we will get FLOOXS installed/running via a Singularity instance on a production level compute system. We will target the UM-System Lewis computer first and then other compute resources as needed. Once the singularity system is in place, the effort required to port the software to other systems will be trivial, which is the main reason for putting in the effort up front. Then, we will repeat previously demonstrated TCAD simulations to explore the capabilities of FLOOXS and further identify any possible deficiencies. We will learn the scripting interface so as to be able to modify demonstration simulations. Then, we will modify material definition parameters to understand the magnitude of the material effects on the demonstration simulation results. After that, we will modify the device models themselves to isolate and minimize any potential simulation artifacts due to device geometry. Simultaneously with that activity, we will invest time to study and understand the underlying mathematical formulations used in FLOOXS and perform an extensive literature review to understand state of the art for integration of other codes into FLOOXS material models. As that effort progresses, we will integrate and augment the FLOOXS materials database with *ab initio* and molecular dynamics tools. We will begin with the use of trivial models (which are mostly made already) and determine the extent to which they can be used to guide above parameter selection. Then, we will identify which models

really need to be made and why. (I.e., when the limits of the basic models are understood with respect to their ability to inform the TCAD simulations, then it will become possible to know what new models will be needed.) Moving on from the trivial models we will make trial models that contain more sophisticated material structures. We will then work to refine the models and compute relevant the fundamental properties (e.g. band structure with defect states, optical absorption properties, and phonon spectrum). Those results will be included into the FLOOXS material database so that device properties can be computed. This will set the stage for optimization processes and more specialized material properties calculations (e.g. electron-phonon coupling and scattering parameters for full-band Monte Carlo simulation) in subsequent years.

2) Small Unmanned Aerial Vehicle Testing and Design of Experiments

Over the past year the UAV team has: created a UAV hardware and software platform capable of providing real-time sensor quantities, integrated the UAV system with a custom HPM source automation platform, and conducted nearly 1400 HPM tests at four facilities around the country. Below is a detailed summary highlighting each aspect of the UAV and HPM testing effort.

A. UAV Diagnostic System Development

SECTION REMOVED

See ***ONR Short Pulse Research, Evaluation and non-SWaP Demonstration for C-sUAV Study:*** *Annual Report Appendix 2018*

B. UAV GTEM Testing

SECTION REMOVED

See ***ONR Short Pulse Research, Evaluation and non-SWaP Demonstration for C-sUAV Study:*** *Annual Report Appendix 2018*

C. Data Analysis and Effects Results

SECTION REMOVED

See ***ONR Short Pulse Research, Evaluation and non-SWaP Demonstration for C-sUAV Study:*** *Annual Report Appendix 2018*

D. Ongoing and Future Research Plan

SECTION REMOVED

See ***ONR Short Pulse Research, Evaluation and non-SWaP Demonstration for C-sUAV Study:*** *Annual Report Appendix 2018*

Adaptive Experimental Design

There has been, an ongoing effort to use classification modeling techniques to map waveform parameters to level of effect on the UAV. The resulting classification model can be used to predict the optimal waveform parameters. Optimal in this sense meaning the waveform parameters that require the lowest amount of power on target to achieve an effect on the UAV. The predicted waveform parameters will then be experimentally tested and the result will be used to update the classification model. In this way, the experimental design adapts using the classification model as the basis for choosing the next set of waveform parameters to test for effectiveness on the UAV. This methodology is being used in pursuit of converging on an optimal set of waveform parameters in an efficient manner. Benchmark testing will be conducted with an analog system, and previously collected GTEM data will be used to further inform the design approach.

Expanded Test Platforms

As the program moves forward, it is important to correlate effects seen on the custom system (Navio 2) with other COTS devices under test. GTEM tests will be conducted using different COTS UAV such as DJI, Pixhawk and Parrot Bebop to determine sensor susceptibilities and how they compare to the custom system. Other systems to be tested are single board IMUs, cameras and gimbals to produce an overall level of lethality effects table, Figure 15.

3) Positive Feedback Non-Linear Transmission Lines (NLTL)

During the last twelve months, we have developed a positive feedback power amplifier coupled with a nonlinear transmission line to generate sustaining high power radio frequency pulses. We have developed a closed-loop network containing a 1500 W (continuous) rated LDMOS (BLF188XR) based power amplifier coupled with a 9-section 1200 V rated schottky diode (STPSC2H12D) based NLTL. The same amplifier can easily produce power bursts of over 10 kW. We have performed several closed-loop experiments at low voltage level (RF input signal amplitude 2 V peak to peak) within a frequency range of 5 MHz to 70 MHz in two configurations, and achieved continuous RF signal outputs with positive gain at different stages of the NLTL (Figures 16 and 17).

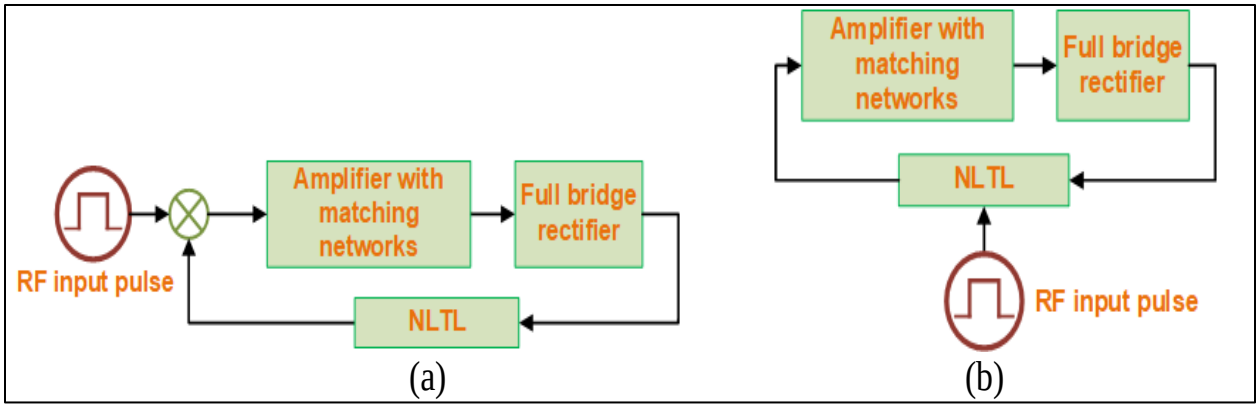

Figure 16. *Simplified block diagram of the (a) first experimental setup (b) second experimental setup.*

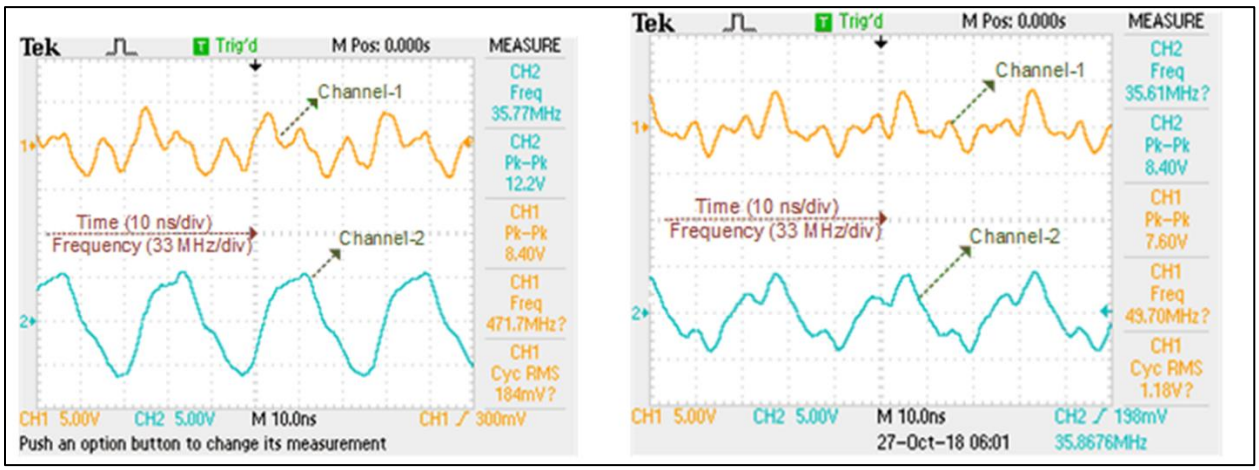

Figure 17. *Generated sustaining RF signal (shown in Channel -1) in (a) first closed-loop configuration (b) second closed-loop configuration.*

A. Major Challenges and Measures Taken

The operation of a non-linear transmission line (NLTL) substantially depends upon the non-linear characteristics of the capacitors used in the NLTL circuit. We have explored capacitance vs voltage (C-V) characteristics of many commercial discrete components to fabricate an effective NLTL. We have identified several schottky diodes, varactors, and ceramic capacitors as potential non-linear capacitive elements of the NLTL. However, capacitance nonlinearity of the commercial components decreases as the applied voltage approaches several kilovolts. Identifying commercial discrete components that can exhibit significant capacitive nonlinearity in the range of kilovolts has been a major challenge in the development of NLTL. 1200 V rated schottky diodes (STPSC2H12D), 1700 V rated bare-die schottky diodes (CPW3-1700-S025B), and 1000 V_{DC} rated class-2 Y5R ceramic capacitors (F472K75Y5RN83K0R) have been selected as the primary components for NLTL fabrication. A 9-section 1200 V schottky diode based NLTL and a 9-section 1000 V_{DC} rated ceramic capacitor based NLTL have been fabricated and tested in our lab. The prototypes are illustrated in Figure 18.

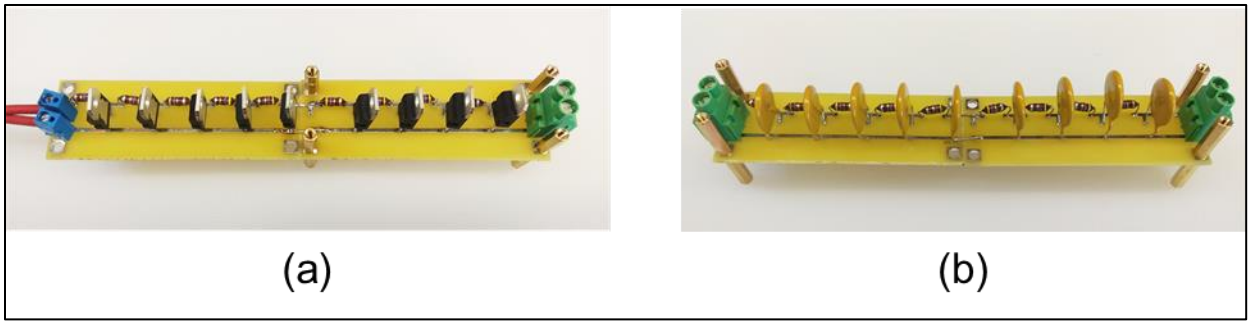

Figure 18. *(a) A Schottky diode based NLTL (b) A ceramic capacitor based NLTL.*

Designing a power amplifier with suitable matching networks to ensure steady gain in the frequency range of 5 MHz to 100 MHz has been one of our initial research objectives. Designing matching networks for a wide frequency range at a center frequency in the range of tens of MHz has been a challenging task for us. We have started using ADS, Genesys and Optenni Lab software to simulate reflection parameter coefficient (S_{11}) and transmission parameter coefficient (S_{21}) of different matching network configurations to mitigate the challenge. At present, we are using Optenni Lab to simulate the performance of different matching network configurations. Our first power amplifier prototype was based on class B topology in the frequency range of 1 MHz to 30 MHz. However, a narrow bandwidth of about 4 MHz has limited the bandwidth of the amplifier. We have modified the matching network design, bias network design, and thermal design for our second power amplifier based on a 1500 W (continuous) rated LDMOS (BLF188XR) to overcome the limitations of the first prototype. We have performed initial open loop experiments with the amplifier coupled with a 1500 W rated 50-Ω dummy load.

A feedback network has been used in the bias circuit to maintain a flat gain within a frequency range of 5 MHz to 70 MHz. The power amplifier has demonstrated voltage gain of about 20 dB to 28 dB within a frequency range of 5 MHz to 70 MHz. The initial closed-loop experiments using the power amplifier coupled with a 9-section NLTL have not produced significant RF signals propagating through the NLTL. Bipolar RF pulses generated by a step-down transformer in the output-matching network of the power amplifier has been responsible for this scenario. We have incorporated a full-bridge rectifier network at the output of the transformer to provide unipolar input RF pulse to the NLTL to mitigate the problem. One of our experimental closed-loop configurations is illustrated in Figure 19.

Experiences

Research activities in the last year has prompted us to understand the non-linear capacitance characteristics of several discrete components better. We are now investigating the availability of commercial non-linear Schottky diodes with greater breakdown voltage (5 kV – 15 kV rated). At present, we have a better understanding of matching network design of power amplifier for maximum power transfer through practical design and software simulation. We have modeled several NLTL's in LTSpice to observe the impact of NLTL length, non-linearity of capacitor, and RF pulse parameter variation on soliton generation. The simulated and experimental outputs from a 9-section Schottky

diode based NLTL in response to different input voltage levels generated by a rapid capacitor charging unit (RCC) are illustrated in Figure 20.

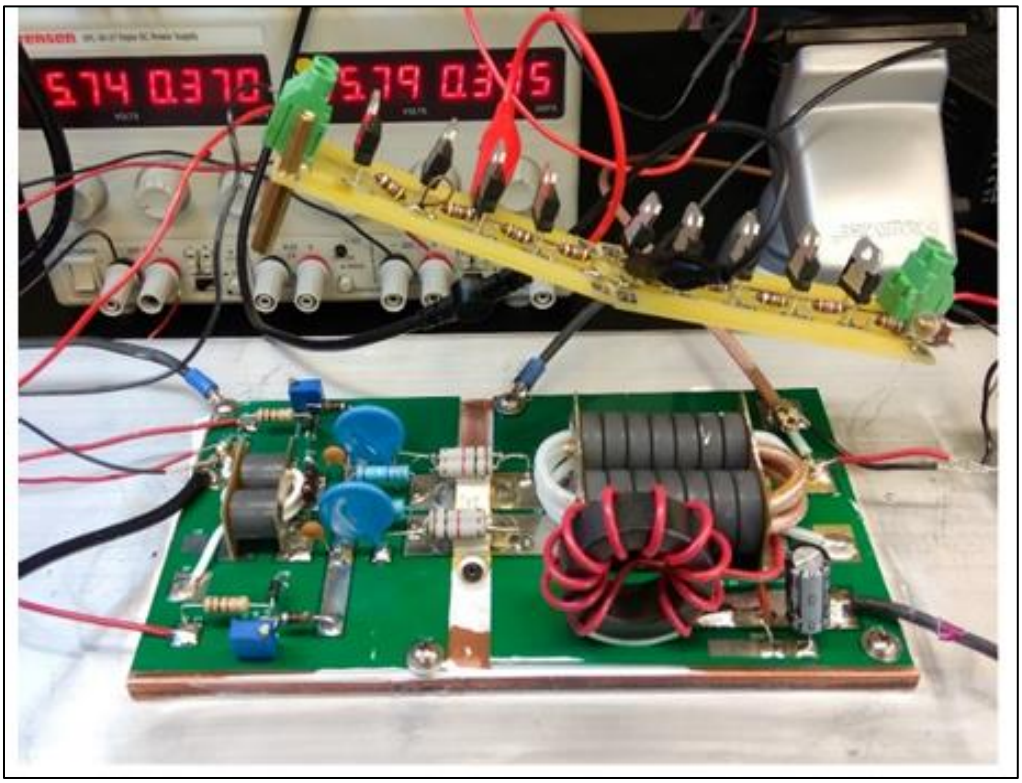

Figure 19. *Experimental setup of the NLTL-amplifier closed-loop configuration.*

In addition, we have simulated the open loop and closed-loop experiment setups using the power amplifier and NLTL in LTSpice before performing these experiments. Simulation results have provided us with a greater understanding of results obtained in practical experiments. We have started working on scaling up the voltage rating and power rating of NLTL. A new 16-section high voltage (3 kV rated) NLTL PCB layout has been designed in Eagle Cad. Multiple 50 Ω RF connectors have been attached with different sections of the NLTL in the design. This feature will allow us to reconfigure the interconnection between the amplifier and the NLTL, and 50 Ω connectors will minimize reflection.

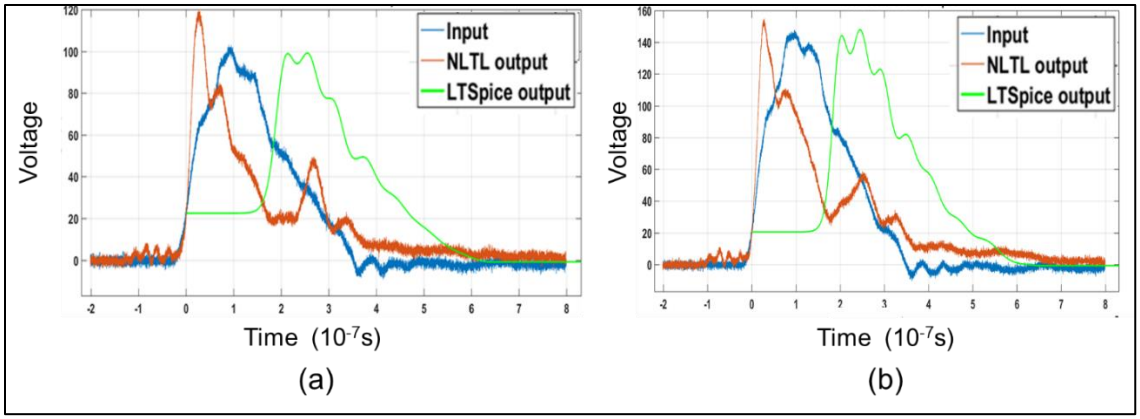

Figure 20. *Responses from the 1200V rated Schottky diode based NLTL's termination load and comparison with LTSpice for (a) 50V input pulse and (b)75V input pulse.*

B. Future Plans

- A power amplifier will be designed that can operate in kV range with a small bias current within the frequency range of 400 MHz- 600 MHz. This amplifier's peak power will be in the range of tens of kWs. We will perform simulations in the Optenni lab to design suitable matching networks for the amplifier in this frequency range.
- The matching networks will ensure sufficient gain in the specified frequency range to compensate for the attenuation of the RF signal caused by the NLTL. In addition, we will work on a transformer-less matching network design to avoid rectification, and to make the power amplifier more compact.
- We will add adaptive biasing network in the amplifier to suppress unwanted modes of solitons propagating through the NLTL and the amplifier.
- A modular ring-shaped high voltage NLTL will be fabricated that can operate in the target frequency range. The power amplifier will be inserted at the center of the ring with a large heatsink attached to it. The entire arrangement will be immersed in an electrically insulating liquid for efficient cooling of the entire package.
- We will use the RCC unit generated high voltage pulse as the input excitation of the high voltage and high power closed-loop NLTL-amplifier network. In our future design, there will be a provision of generating the high voltage impulse on-board.

4) Applied RF Coupling Simulation and Modeling of sUAV

Quantifying the electromagnetic response of sUAVs is complicated by the wide variety of their shapes, sizes, and material compositions. A wide range of electronics, subsystems and components can also be featured in sUAVs. Therefore, over the first year of the project we accomplished the following milestones:

- Reviewed common sUAV shapes, sizes, material compositions, and electronics.

- Used Characteristic Mode Analysis (CMA) to computationally quantify electromagnetic coupling and interference to UAV frames over the L-band and S-band.
- Validated the CMA coupling predictions using experimental measurements conducted by our collaborators at the Electromagnetic Compatibility Laboratory at Missouri University of Science and Technology.

CMA decomposes the total currents induced on any scatterer due to a particular excitation in terms of a set of fundamental modes. It also provides the relative significance of each mode at a certain frequency. Therefore, within a frequency band of interest, we can only focus on the modes that are significant, neglect the insignificant modes, and use these modes to quantify and compare the electromagnetic response of sUAVs with different properties. Moreover, CMA provides the radiation characteristics for each mode, identifying the optimum incident fields to excite or suppress a particular mode. Therefore, CMA will facilitate analyzing the electromagnetic response of the wide variety of sUAVs to be analyzed in this project. The accomplishments achieved in each of the above milestones are detailed in the following subsections.

A. sUAV Shapes, Material Compositions, and Electronics Review

Shapes

The fundamental modes of a structure have a high dependence on the symmetry of the structure. Therefore, we decided to review all common UAV shapes and identify their associated symmetry. Some of the common UAV shape categories are shown in Table 2. So far we have been focusing on studying quadcopters. Future work will include updating our CMA for the other shapes in Table 2.

Table 2. *Common sUAV shapes.*

UAV Family1	Shape	UAV Family1	Shape	UAV Family2	Shape
Tricopter		X8		Delta Wing	
Y6		Hexacopter		Motorized Sailplane / Glider	
Quadcopter		Octocopter		Skywalker	

Material Compositions

A wide variety of materials have been reported for sUAV frames. These materials include: 1) good conductors (such as Aluminum and Titanium alloys), *2*) weak conductors (such as carbon-fiber based composites), and *3*) dielectrics (such as wood and plastics). Some of the common sUAV materials are summarized in Table 3 below. So far, we have performed CMA of sUAVs composed of perfect electric conductors (PEC) and sUAVs composed of dielectric such as Nylon 66.

Table 3. *Common sUAV materials.*

Material	References
Balsa wood Plywood	[1]-[2]
Fiberglass	[2]-[3]
Aluminum	[4]
Titanium Alloys	[5]
Carbon Fiber	[5]

Electronic Components

Over the last year, we reviewed the electronic components used in UAV's as reported in the literature. Our goal was to identify the most common electronic components that are critical to the functionality of UAVs and focus on analyzing the effect of different electromagnetic waveforms on the operation of these components. Table 4, below, compiles the components we have identified so far. They are arranged in descending order of how many times each electronic component was reported in the literature. Future work will include developing a plan to test the electromagnetic susceptibility of these chips.

Table 4. *List of common UAV electronic components.*

Component	Component Type	Manufacturer	# of Appearances	Appeared in
MS5611	Barometer	TE Connectivity	12	[6]-[13].[18]-[21]
MPU-6000	Accelerometer & Gyroscope	TDK InvenSense	10	[7][9],[12],[14],[16],[18]-[19],[23]-[25]
STM32F427	Microprocessor	STMicroelectronics	7	[10],[13],[15],[18]-[21]
STM32F103	Microprocessor	STMicroelectronics	7	[7],[13],[15],[18]-[20],[26]-[27]
MPU-9250	MCM (accel,gyro,magnet)	TDK InvenSense	6	[6],[9]-[10],[13],[16]
HMC5883	Magnetometer	Honeywell	5	[7]-[9],[11],[16]

LSM303D	Accelerometer & Magnetometer	STMicroelectronics	4	[10],[12],[18],[19]
L3GD20	Gyroscope	STMicroelectronics	4	[10],[12],[18],[19]
STM32F	Microprocessor	STMicroelectron	4	[7],[23]-[25]
STM32F303	Microprocessor	STMicroelectronics	4	[11],[14],[17],[22]
MPU-6050	Accelerometer & Gyroscope	TDK InvenSense	4	[7],[11],[17],[24]
NEOM8F3	GPS Module	U-Blox	2	[6][9]
ITG3205	Gyroscope	TDK InvenSense	2	[8],[17]
ICM20608	Accelerometer/Gyroscope	TKS InvenSense	2	[13],[21]
BMP085	Barometer	Bosch Sensortec	2	[7],[16]
BMA180	Accelerometer	Bosch Sensortec	2	[8],[17]
LC1860	CPU	Leadcore Technology	2	[26]-[27]
LC1160	Power Management Unit	Leadcore Teachnology	2	[26]-[27]
MA2155	Vision Processing Unit	Movidius	2	[26]-[27]

B. Characteristic Mode Analysis of UAV frames

Simple PEC UAV shapes

UAV are typically composed of many different components with each component contributing to the overall electromagnetic response. Modeling the entire UAV with all of its components, will lead to a convoluted electromagnetic response and it will be hard to isolate the contribution of each component in the overall electromagnetic response. Therefore, as a starting point we divided the UAV into components and studied each component individually. Since the frame is typically the largest component of the UAV, it will dominate the response at low frequencies, therefore we started by studying the electromagnetic response of UAV frames. We started our analysis with the simple quadcopter UAV shown in Figure 21. The frame can be simplified and modeled as two intersecting identical bars. Therefore, decomposing the frame into two bars and studying each bar separately to clarify the total behavior of the frame. Perfect electric conducting material was assigned to the frame to simplify the CMA.

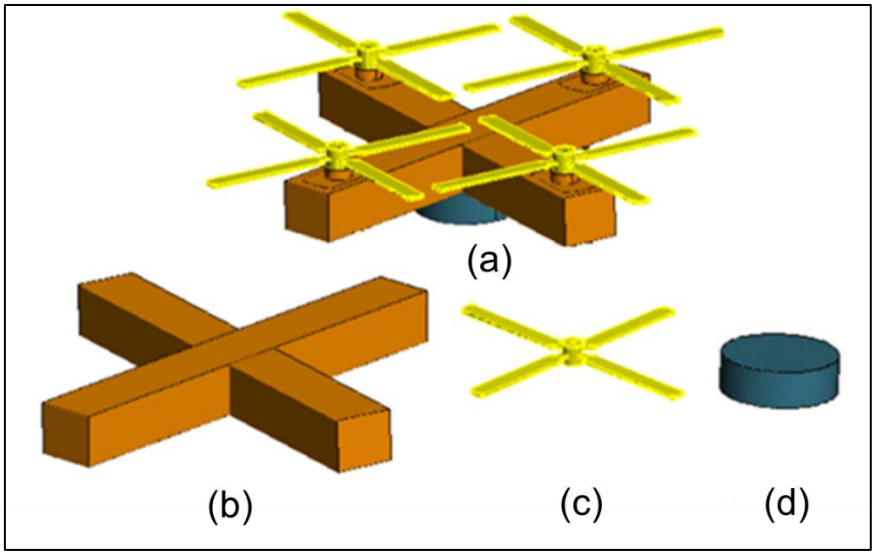

Figure 21. *(a) Full UAV design, (b) UAV frame, (c) UAV blades , and (d) UAV transmitting and receiving system.*

Figure 22 shows the fundamental modal currents of a single PEC bar with dimensions 0.2 m, 0.028 m, and 0.024 m. The red areas indicate maximum currents locations or hot spots whereas the blue regions show currents with low magnitudes. It is clear from Figure 22 that one of the dimensions (x-axis) of the bar is significantly larger than the other two, indicating that this dimension will dominate the low frequency response. Alongside this dimension, the fundamental modal currents follow a pattern that is very similar to sin (ℓ), sin (2ℓ), and sin (3ℓ) where ℓ is the normalized length of the bar along the x-axis such that $0 < \ell < 1$ [28], [29]. Alongside the other two dimensions, the modal currents are approximately uniform due to their small sizes. However, if the frequency is increased such that the wavelength of the incident wavelengths starts to become comparable to the two other dimensions of the bar, then we will also see additional fundamental modes along the y and z directions of the bar. At any frequency between 0 GHz and 3 GHz, the current generated on the bar will be composed of a weighted sum of the three modes in Figure 22. The weight of each modes is determined by two factors. The first factor is termed the modal significance, shown in Figure 23, and it represents the relative importance of a certain mode at a desired frequency and it is a function of the shape, material, and the environment of the object but it is completely independent on the incident field excitation. The second factor, termed the modal excitation coefficient, measures the level of coupling between a certain incident electric field and a certain mode.

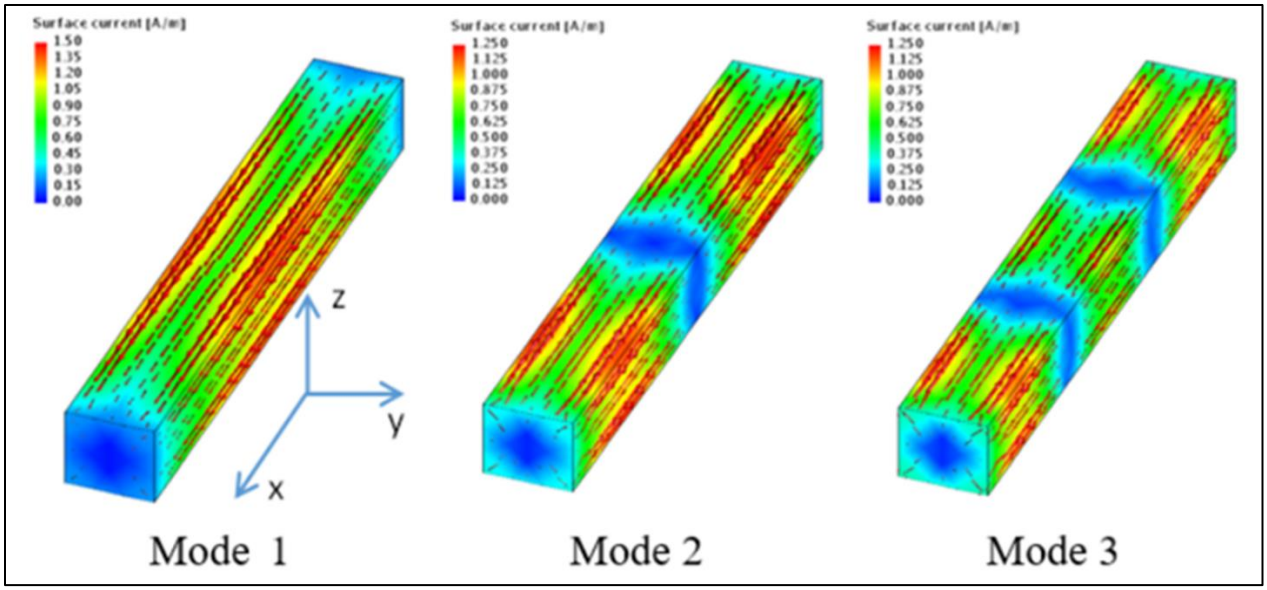

Figure 22. *Modal currents of single PEC bar.*

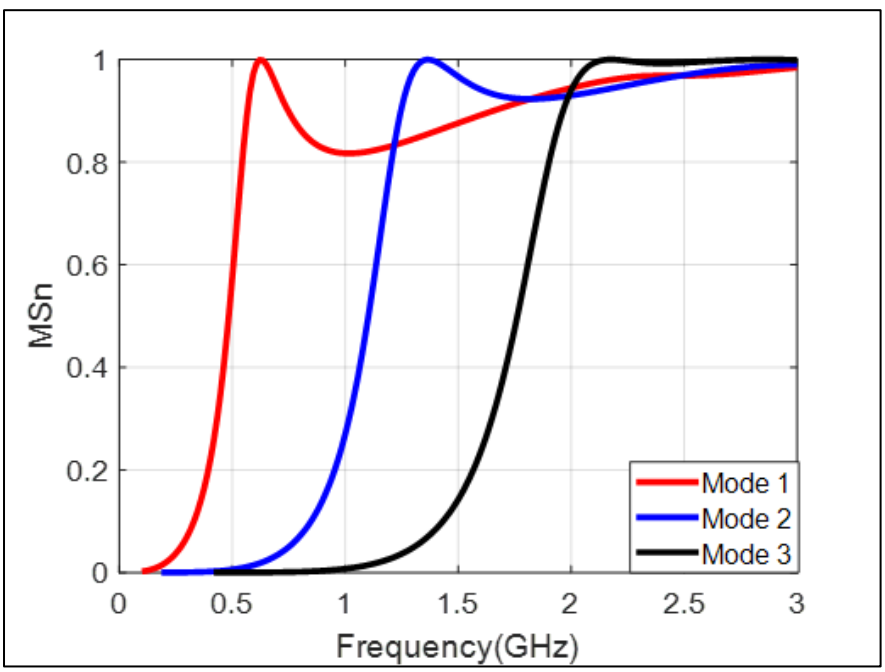

Figure 23. *Modal significance (MSn) of single PEC.*

Figure 23 shows the Modal Significance of the PEC bar in Figure 22. At a certain frequency, the Modal Significance in Figure 23 provides the relative importance of each mode. For example, at 0.68 GHz mode 1 has a significance of 1 whereas all the other modes have a significance below 0.05. This means that up to 0.67 GHz the response is dominated by mode 1 and the total current excited on the bar will be very similar to the mode 1. Therefore, an incident electromagnetic wave will only couple to the bar if its field distribution will couple to mode 1. Beyond a frequency of 0.67 GHz, other modes start to become significant and the response will be due to a mixture of modes based on the

relative importance of each mode at a certain frequency and whether the incident wave excites a certain mode or not.

As we mentioned, the single bar was the first step to construct the frame of the quadcopter UAV. Two identical bars in a cross formation were constructed to construct the UAV frame in Figure 21 (b) and the CMA performed for the new structure. We anticipated that we will achieve similar modes to those in Figure 22 as well as additional modes due to the coupling between the two bars. Figure 24 shows the first six modes of the cross-shaped UAV frame and Figure 25 shows the corresponding modal significance.

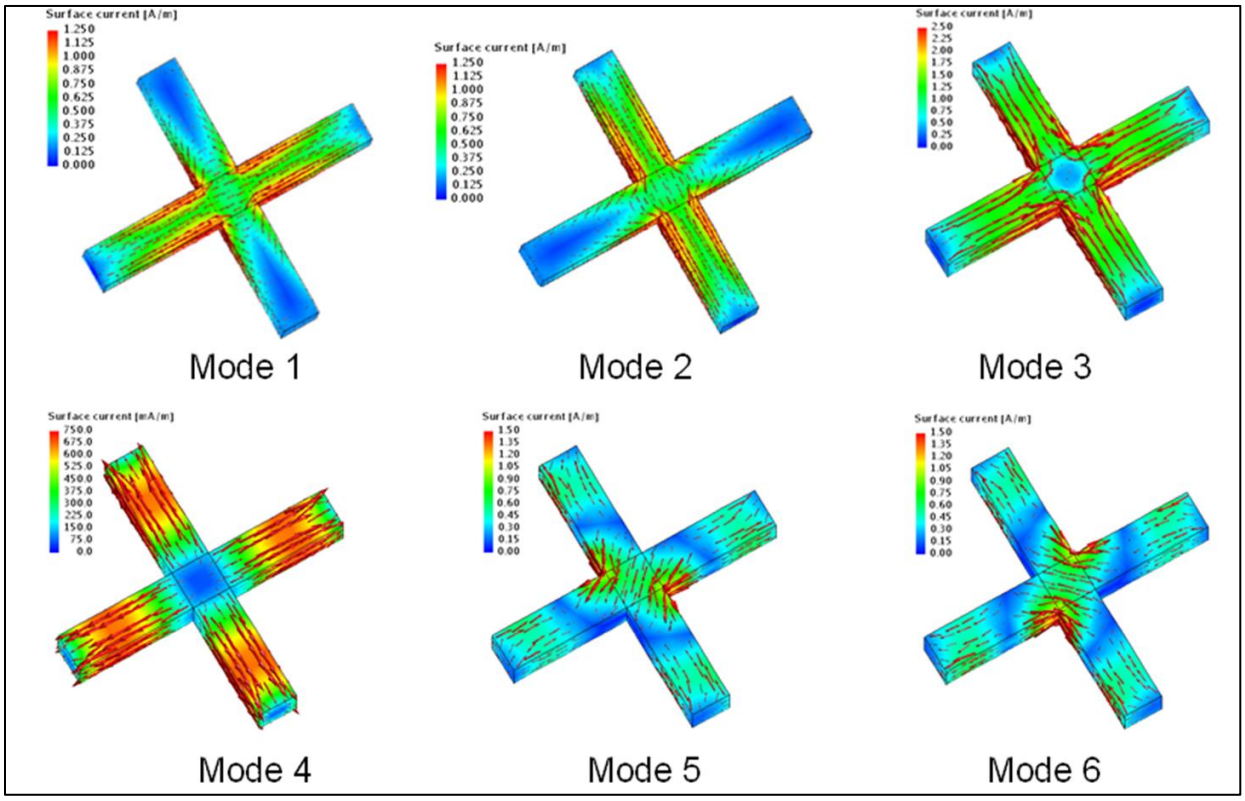

Figure 24. *Fundamental modes of a PEC cross-shaped UAV frame.*

Mode 1 and Mode 2 have overlapping modal significance as shown in Figure 25 which indicates that they have equal significance at every frequency. This overlap arises from the symmetry of the structure and the identical dimensions of the two intersecting bars. That is, in Mode 1 only the horizontal bar will exhibit significant currents whereas in Mode 2, only the vertical bar will exhibit significant currents as shown in Figure 24. Therefore, Mode 1 will be excited if the incident field is parallel to the horizontal bar, Mode 2 will be excited if the incident field is parallel to the vertical bar, and a circularly polarized wave will excite both modes. If the two bars had different dimensions, the modal significance of Mode 1 and Mode 2 will not overlap. Mode 1 and Mode 2 have a similar distribution to Mode 1 of the isolated bar in Figure 22. The hot spots, shown in red in Figure 24, indicate the areas with the maximum currents which will be the areas with maximum fields scattered and the UAV electronic devices near these spots will be more prone to coupling.

Modes 3 is a hybrid combination of Mode 1 and Mode 2 and they resonate at higher frequencies as shown in the green Modal Significance curve in Figure 25. Modes 5 and 6 also overlap as their current pattern is similar but rotated by 90.

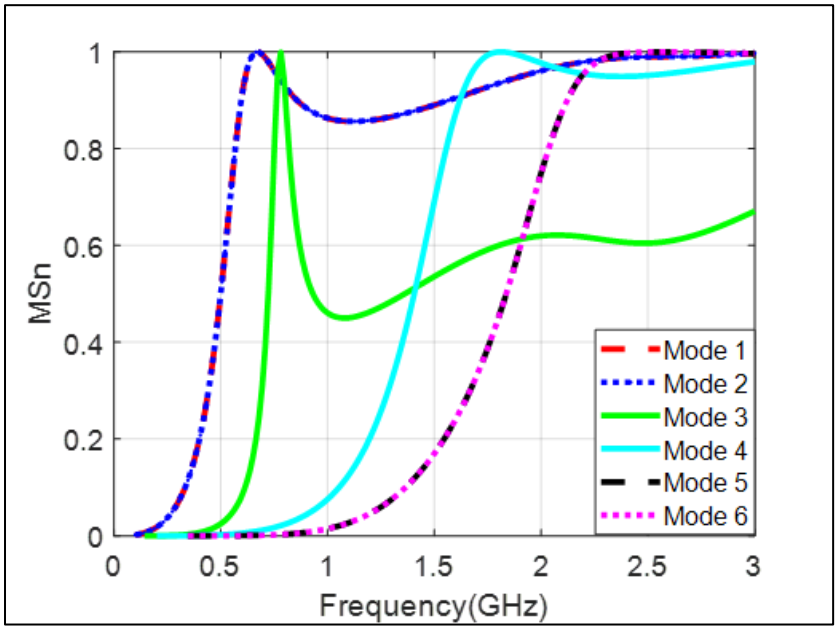

Figure 25. *Modal significance of a PEC cross-shaped UAV frame*

Realistic PEC UAV Shapes

Figure 26*. Makerbot Digitizer 3D Scanner*

Moving on to realistic UAV three-dimensional 3D shapes, we used the MakerBot Digitizer scanner to scan the frame of the model UAV developed by Caruso's group. A picture of the scanner is shown in Figure 26. Using the MakerBot Digitizer scanner, we developed 4 different 3D versions, V1-V4, of the UAV with V1 being the coarsest whereas version 4 is the finest as shown in Figure 27. That is, version 4 is the most accurate scanned structure and it includes most of the features of the actual UAV frame. As a starting point, we will assume that all frames are perfect electric conductors but we will study frames

with more realistic dielectric properties in the next section. Each version, will have a different current distribution for the dominant 1st mode as shown in Figure 28. The geometrical differences between the versions will affect the current distribution of Mode 1 affecting the coupling to wires and electronic chips at different locations above the frame.

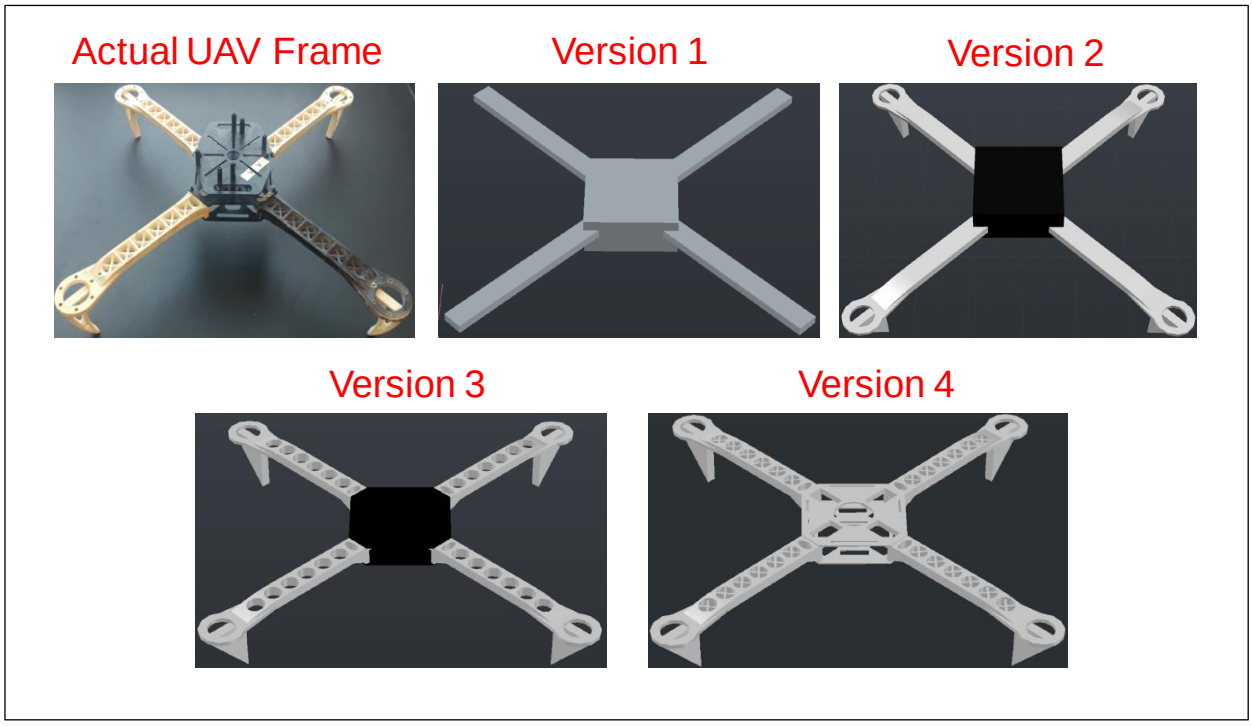

Figure 27. *The actual frame of the UAV and four different 3D representations of its geometry.*

To demonstrate how the relative location of a wire can affect the coupling current, we studied coupling to four identical wires at different locations above Version 1 of the UAV. The incident electric field is oriented parallel to wires 1, 2, and 3 and perpendicular to wire 4 as shown in Figure 29a. Figure 29b shows the current distribution of Mode 1 to clarify that the hotspots are near the arms and not the central part of the UAV. Figure 29c shows the coupled current at the center of each of the 4 wires. The coupling current to wire 4 is the lowest as expected since this wire is perpendicular to the applied field. Wire 1 and Wire 3 show higher overall coupling current than Wire 2 because they are above the "hotspots" of Mode 1 shown in Figure 29b. The coupling current to Wire 2 is lower than that of Wires 1 and 3 because it is not located near the hotspot of Mode 1 as shown in Figure 29b.

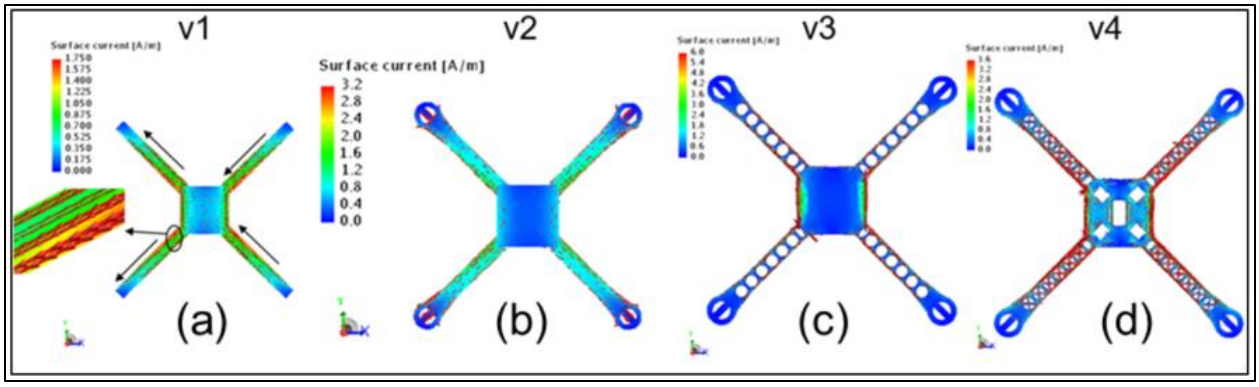

Figure 28. Current distribution of mode 1 for different scanned versions of UAV.

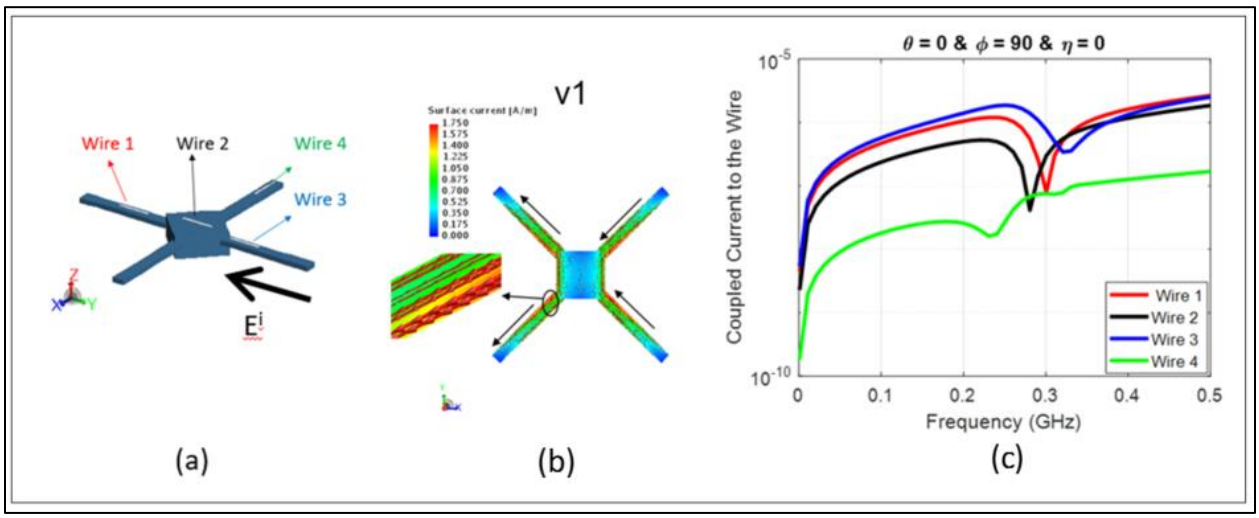

Figure 29. (a) Wiring system above a PEC frame (V1) and the applied electric field orientation (b) current distribution of Mode 1, and (c) coupled current of the wires above the PEC UAV frame.

Realistic Dielectric UAV Shapes

In the last section, we applied CMA to the 3D scanned versions of the UAV frames assigning perfect electric conductor to their material. One of the main conclusions, is that for the first mode the hot spots are located near the arms of the frame. We illustrated that the wires mounted above the hot spots on the arms will couple more than the wires at the middle part of the UAV accordingly. If the wire is placed above the central part of the metallic frame it will have lower coupling because no modes are existing at this part of the UAV at low frequencies.

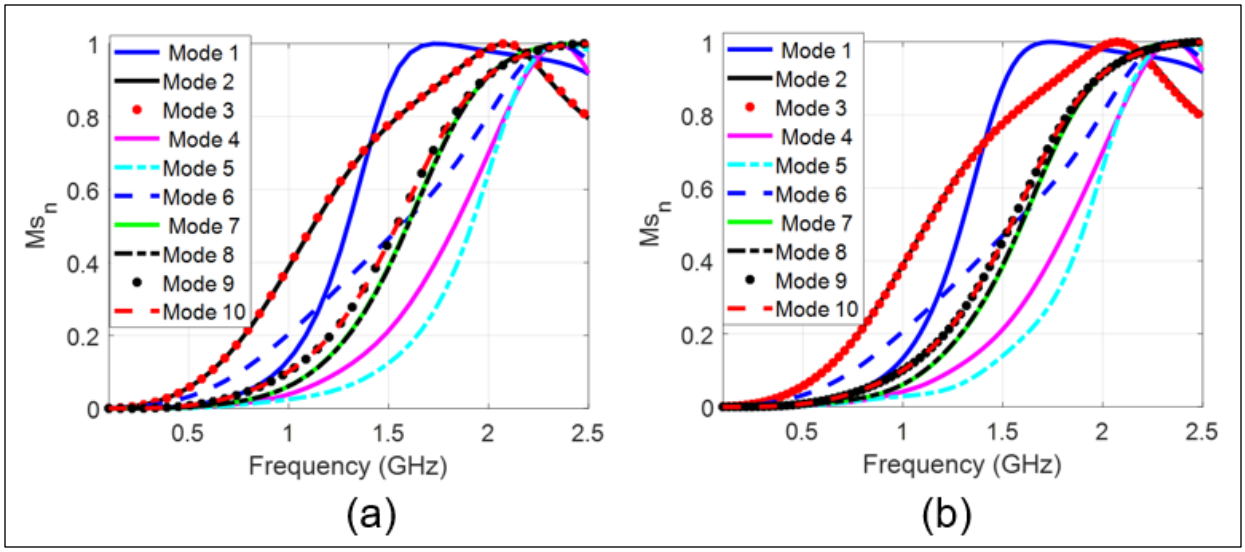

Figure 30. *Modal significance of a dielectric UAV frame (a) The 1st version (b) The 2nd version.*

In this section, we performed CMA to the first two representations of the scanned UAV model in Figure 27 but we changed their material properties to match the realistic dielectric properties of common UAV frame plastics ($\varepsilon_r \approx 3.3$ "Nylon 66"). The Modal Significance of the two versions is shown in Figure 30. The modal significance of both versions is identical while version 2 has extra pieces at the arms of the UAV which illustrates that the response of the dielectric UAV frame is less sensitive to the physical features of the arms.

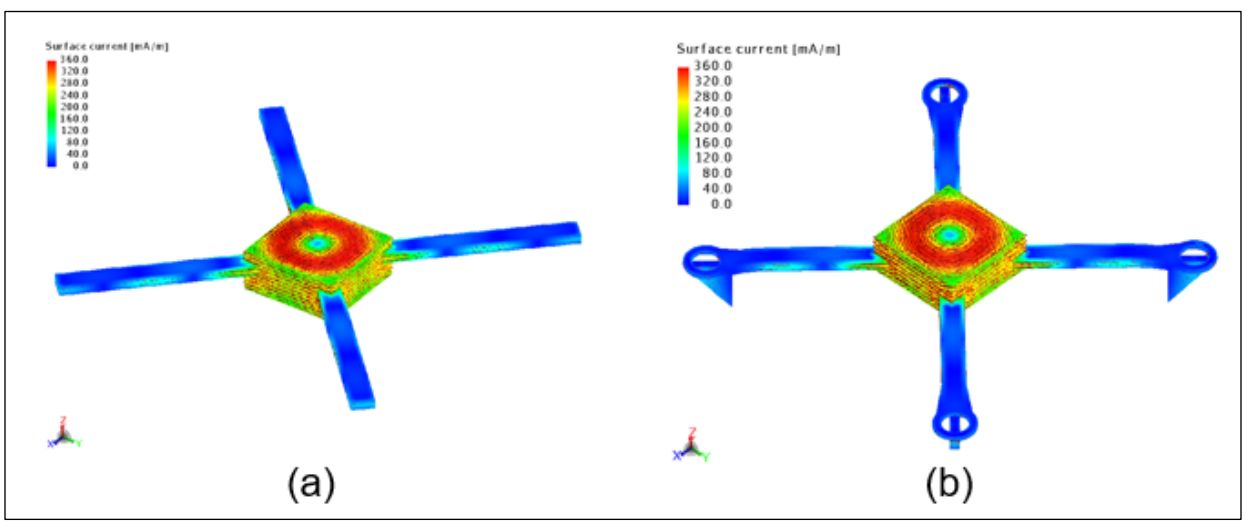

Figure 31. *Mode 1 current distribution over (a) The 1st version (b) The 2nd version of the dielectric UAV.*

The modal current distributions of both versions of the UAV are shown in Figure 31. The current distribution of the first mode is concentrated at the central part of the frame not at the arms. Therefore, changing the length/width of the arm will have minor contribution to the overall electrical path of the mode current. Which is completely the opposite case of

the conducing frames where we showed that the central part of the frame will have the minor contribution to mode behavior.

Similar to our previous discussions about the mode hybridization phenomena, the modal currents of Mode 2 and Mode 3 are identical but Mode 3 is rotated by 90° around the axis of UAV in comparison to Mode 2. Mode 4 is a hybrid combination of Mode 2 and Mode 3. As shown in Figure 31 and 32, it is clear that if the electronic devices mounted on the central part of the UAV it will be affected when any mode is excited. Therefore, any electronic chips on the central part of the UAV may be prone to coupling and interference. To demonstrate how the relative location of the wire can affect the coupling current, we studied coupling to four identical wires, wire length = 6.5 cm, wire radius= 0.25 mm, wire height above the frame = 0.2 mm, at different locations above Version 1 of the UAV.

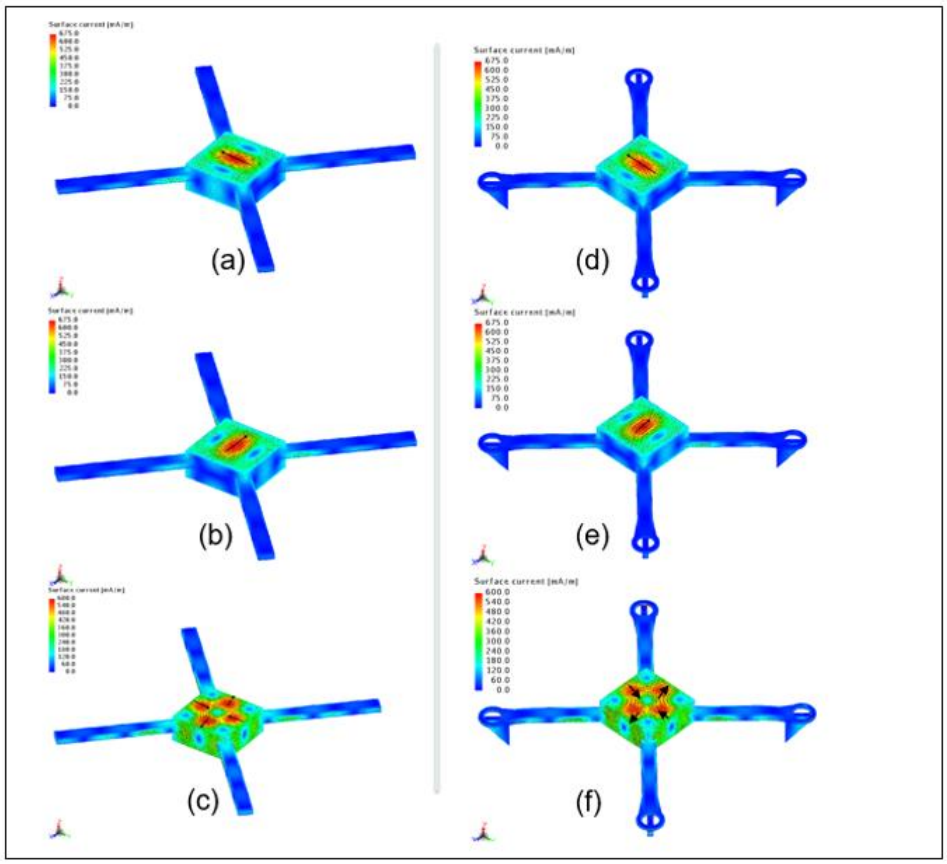

Figure 32. *Current distribution of (a) mode 2, (b) mode 3, (c) mode 4 for the 1st version of the dielectric UAV frame. (d) mode 2, (e) mode 3, (f) mode 4 for the 2nd version of the dielectric UAV frame.*

The incident electric field is oriented to excite Mode 2 of the frame and parallel to all the wires 1 as shown in Figure 33a. Figure 33b shows the coupled current at the center of each of the 3 wires. At 1.5 GHz, Wire 2 has the highest coupled current, which is the opposite of the case of UAV PEC frames. The other peaks of wire 1 and 3 at 2 GHz is corresponding to the resonance frequency of mode 1 of the wire itself. To validate our conclusion, the same wires setup was simulated in free space and the comparison

between the coupled current to wire 2 in free space and above the dielectric frame is shown in Figure 34.

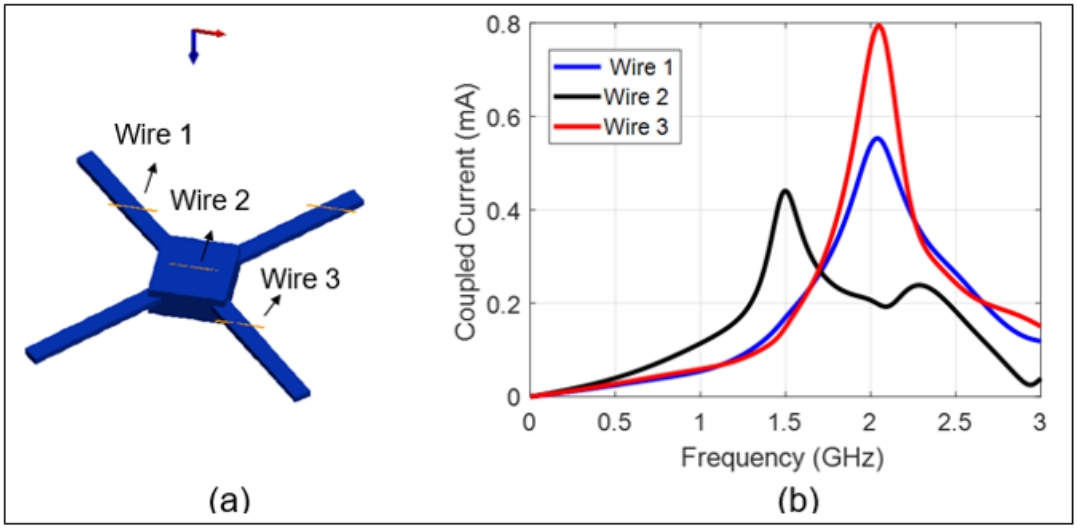

Figure 33. *(a) Wiring system above a dielectric frame (V1) and the applied electric field orientation (b) Coupled current of the wires above the dielectric UAV frame.*

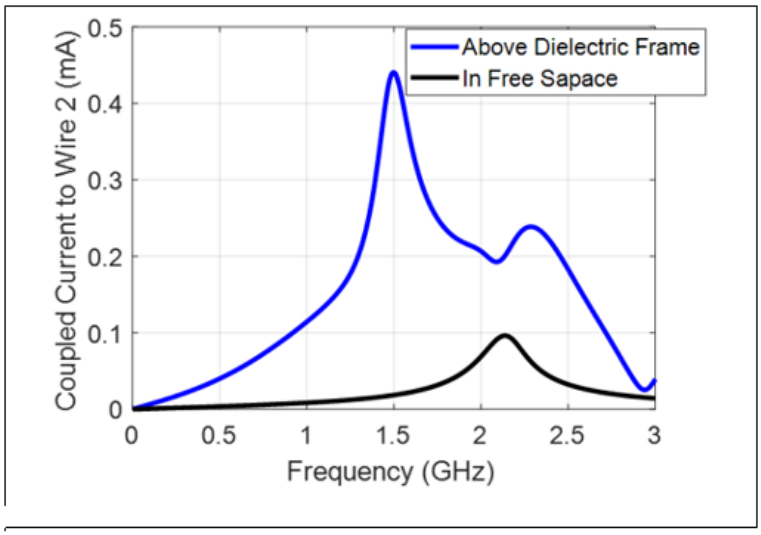

Figure 34. *Comparison between the total coupled current to wire 2 above the dielectric UAV frame and in free space.*

C. Experimental Verifications of CMA results

As part of our collaboration with Professor Beetner's group at MS&T, experimental measurements of the coupled current to simple UAV frames were conducted. Figure 35a and Figure 35b show a sketch and a picture, respectively, of the simple frame model that was used in the experimental measurements. It consists of a square metallic plate connected to 4 wires, to present the arms. The rectangle has a 110 mm edge width and each wire is 190 mm long. The wires form an approximate angle of 135◦ with the edges

of the square plate. In the measurements, the incident electric field was polarized in the direction shown in Figure 35a. A current probe at the beginning of the wire was placed to measure the coupled current induced on each wire. The measured current at each of the 4 wires is shown in Figure 36.

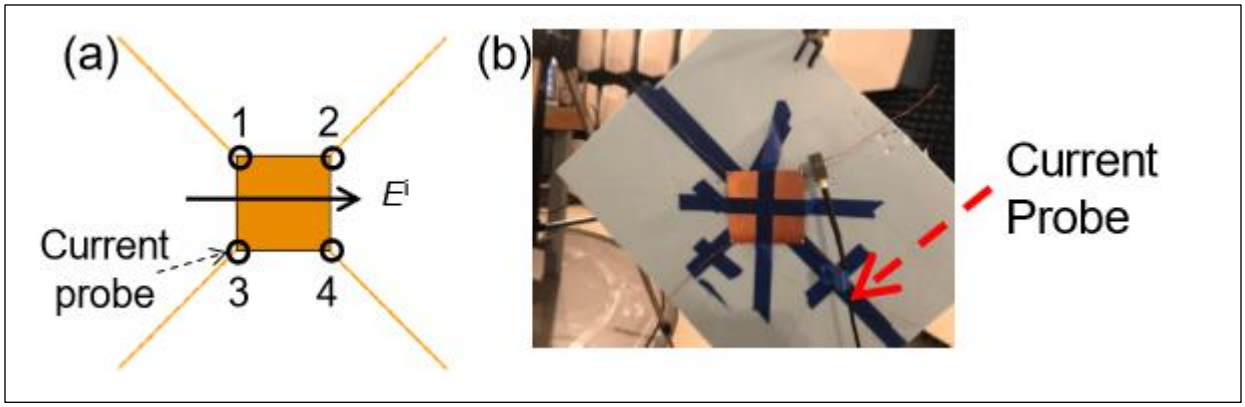

Figure 35. *(a) Sketch of simple UAV frame showing locations of current probes. (b) Experimental setup showing the realized frame and the current probe at one of the four probe locations.*

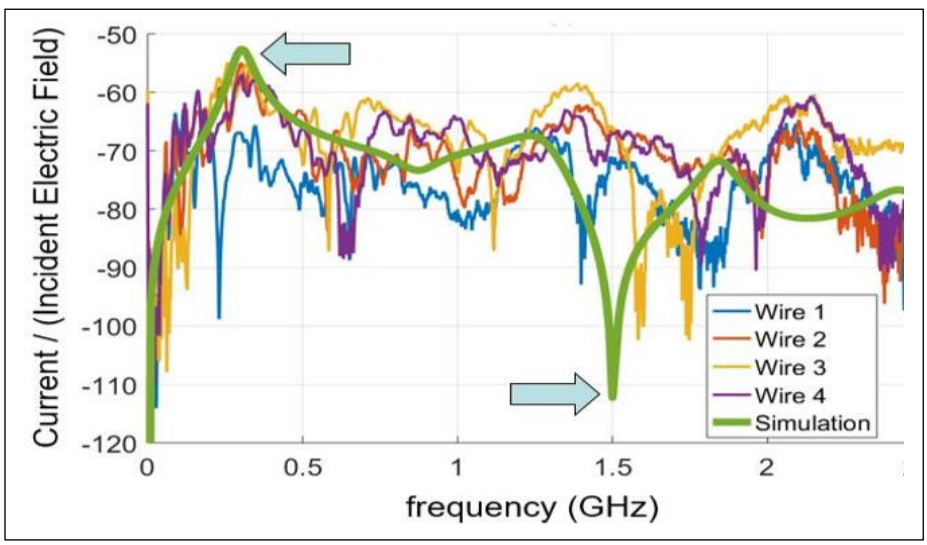

Figure 36. *Measured current of the PEC frame at each wire. (dBA)*

In addition, the coupled current simulated using the commercial electromagnetic solver FEKO is also shown in Figure 36. In the simulations, a perfect electric conductor boundary condition is assigned to all components of the frame. Due to the symmetry of the frame and the excitation, all 4 wires should exhibit the same current. Excellent agreement between the experimental measurements from Wires 2-4 is achieved as shown in Figure 36.

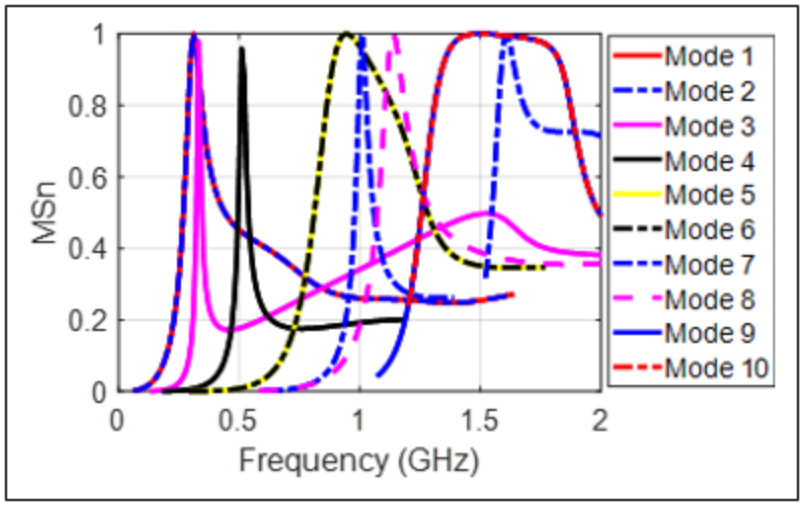

Figure 37. *Modal significance of the UAV.*

The interesting common feature of all the measured currents and simulations is that the coupled current will have a peak around 0.3 GHz and a minimum around 1.5 GHz. However, we need to explain why there is a maximum 0.3 GHz and why we have a coupling minimum at 1.5 GHz. That is, are there no coupling pathways to the UAV's frame at 1.5 GHz and, therefore, it is immune to interference at this frequency? To answer these questions, we applied CMA for this frame. As we mentioned in our previous reports, the CMA is independent of the field excitation and will give an insight of all the supported modes of the structure and how to excite each particular mode. The modal significances are shown in Figure 37 which identifies at each frequency the weight of each mode that can contribute to the total response of the structure. It's clear that at 0.3 GHz Mode 3 is dominant as well as Modes 1 and 2. In the vicinity of the frequency of 1.5 GHz, Modes 9 and 10 are dominating and many other modes have lower significance and therefore can contribute to the response. Therefore, Figure 37 immediately helps us to identify that there are "modes" or coupling pathways to the frame at 1.5 GHz. Therefore, the reason we are seeing a minimum in the coupled current in Figure 36 has to be due to the following two reasons: (i) the incident excitations used in the experiment was not capable of exciting the dominant modes, 9 and 10, at 1.5 GHz and/or (ii) these dominant modes show current maxima at locations different from where the current probe was located on the frame of the UAV. These modes can be excited by varying the incident field excitation to optimize the coupling with these modes.

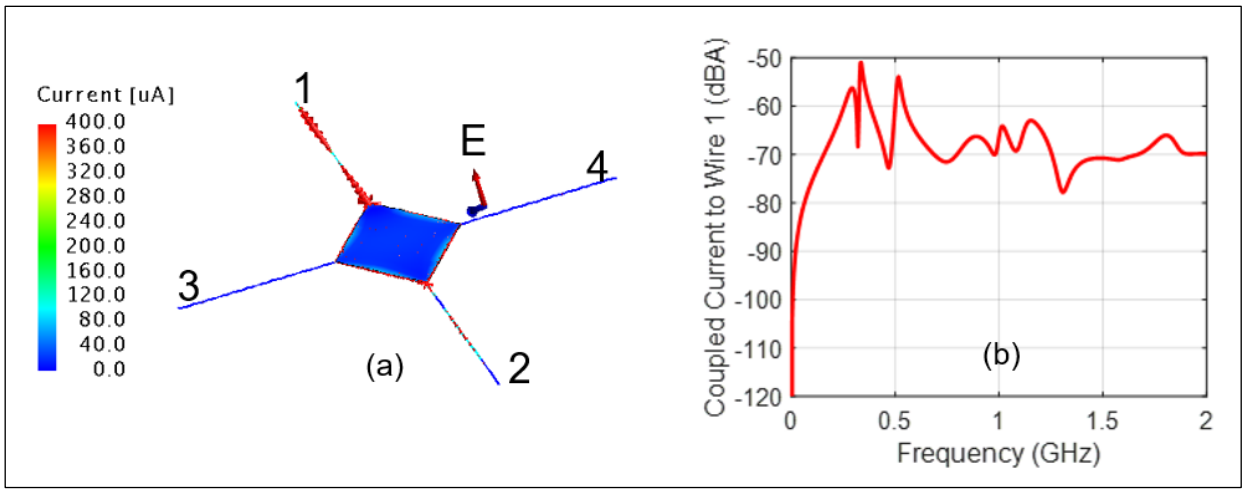

Figure 38. *(a) Total coupled current to the UAV at 1.5 GHz. (b) Total coupled current to the UAV for the oblique incidence.*

To examine the CMA prediction, we simulated the UAV with an oblique incidence electric field shown in Figure 38a and plotted the total current coupled to one arm as shown in Figure 38b. The dip at 1.5 GHz is completely removed because of the excitation of Mode 9.

D. Future Work

The previous sections demonstrated the effectiveness of CMA in predicting the coupling current due to different excitations and in predicting the locations on UAV frames where the coupling will be maximum or minimum. Moreover, we used CMA to quantify the effect of shape and material of the frame on the coupling to UAV wiring systems and electronic components. Our future work will include the following tasks:

- Expand the CMA to include all the materials, sizes, and shapes relevant to UAVs.
- Test the electromagnetic susceptibility of common UAV electronic components.
- Perform an exhaustive statistical analysis of coupling to wires with different lengths, different heights, and different locations above the UAV frames with realistic shapes and dielectric properties.
- Couple the Multi-conductor Transmission Line (MTL) approximation with CMA to predict the coupling current to UAV wire systems given their relative location with respect to the UAV's frame.
- Collaborate with Dr. Zhen Peng at the University of New Mexico to explore different domain decomposition techniques for the efficient CMA of realistic UAVs.

E. Products, Publications, Patents, License Agreements, etc.

a. Title: Electromagnetic Analysis of Unmanned Aerial Vehicles Using Characteristic Mode Analysis
b. Authors: M. Hamdalla, J. Roacho-Valles, J. Hunter, D. Beetner, A. Hassan, A. Caruso
c. Conference Name*: AMEREM*
d. Conference Date: Aug 27-31, 2018
e. Conference Location: Santa Barbra, CA, USA
f. Publication Status: published
g. Publication Date:
h. Publication Identifier Type:
i. Publication Identifier:
j. Acknowledgement of Federal Support?

a. Title: Characteristic Mode Analysis of Unmanned Aerial Vehicles with Realistic Shapes and Material Composition
b. Authors: M. Hamdalla, A. Hassan, A. Caruso
c. Conference Name: IEEE International Symposium on Antennas and Propagation and USNC-URSI Radio Science Meeting
d. Conference Date: July 8-13, 2018
e. Conference Location: Boston, Massachusetts, USA
f. Publication Status: published
g. Publication Date:
h. Publication Identifier Type: NONE
i. Publication Identifier: NONE
j. Acknowledgement of Federal Support? Yes

F. References

[1] D. Erdos, A. Erdos and S. E. Watkins, "An experimental UAV system for search and rescue challenge," in IEEE Aerospace and Electronic Systems Magazine, vol. 28, no. 5, pp. 32-37, May 2013.
[2] G. Pisanich and S. Morris, "Fielding an amphibious UAV: development, results, and lessons learned," Proceedings. The 21st Digital Avionics Systems Conference, 2002, pp. 8C4-1-8C4-9 vol.2.
[3] Anton, Steven Robert. "Multifunctional piezoelectric energy harvesting concepts." PhD diss., Virginia Tech, 2011.

[4] Niethammer, U., M. R. James, S. Rothmund, J. Travelletti, and M. Joswig. "UAV-based remote sensing of the Super-Sauze landslide: Evaluation and results." Engineering Geology 128 (2012): 2-11.

[5] Akshay Balachandran, Divyesh Karelia, Jayaramulu Challa, “M*aterial selection for unmanned aerial vehicle,*” International Journal of Mechanical Engineering and Technology (IJMET),), Volume 5, Issue 8, August (2014), pp. 34-40.

[6] "Emlid Navio2 — Raspberry Pi autopilot HAT powered by ArduPilot & ROS", Emlid, 2017. [Online]. Available: https://emlid.com/navio/. [Accessed: 29- Nov- 2017].

[7] K. Shilov, "The Next Generation Design of Autonomous MAV Flight Control System SmartAP", Department of Aeromechanics and Flight Engineering, Moscow, Russia, 2014.

[8] G. Sun, J. Xie, Y. Li and C. Rizos, "Development of an Unmanned Aerial Vehicle Platform Using Multisensor Navigation Technology", School of Surveying and Spatial Information System, University of New South Wales, Sydney, Australia, 2017.

[9] B. Frazer, R. Lueg, R. Borden and J. Howard, "Dronenet: The Quad Chronicles", Dept. of Electrical Engineering and Computer Science, University of Central Florida, Orlando, Florida, 2017.

[10] "Pixhawk 2.1 Standard Autopilot", Unmanned Tech, 2017. [Online]. Available: https://www.unmannedtechshop.co.uk/pixhawk-2-1-standard-autopilot/. [Accessed: 18- Dec- 2017].

[11] Seriouslypro.com, [Online]. Available: http://seriouslypro.com/files/SPRacingF3-Manual-latest.pdf. [Accessed: 30- Jan- 2018].

[12] 3dr.com, [Online]. Available: https://3dr.com/wp-content/uploads/2017/03/pixhawk-manual-rev7-1.pdf. [Accessed: 30- Jan- 2018].

[13] P. Autopilot, "Pixhawk Mini · PX4 User Guide", Docs.px4, 2018. [Online]. Available: https://docs.px4.io/en/flight_controller/pixhawk_mini.html. [Accessed: 30- Jan- 2018].

[14] "Flight Controllers", Lumenier.com, [Online]. Available: http://www.lumenier.com/products/flight-controllers. [Accessed: 30- Jan- 2018].

[15] "Flight Controllers", Lumenier.com, [Online]. Available: http://www.lumenier.com/products/flight-controllers. [Accessed: 31- Jan- 2018].

[16] "MultiWii 328P Flight Controller w/FTDI & DSM2 Comp.", Hobbyking, 2018. [Online]. Available: https://hobbyking.com/en_us/multiwii-328p-flight-controller-w-ftdi-dsm2-comp-port.html?___store=en_us. [Accessed: 31- Jan- 2018].

[17] "Holybro Kakute v1.0 F3 Flight Controller", Hobbyking, 2018. [Online]. Available: https://hobbyking.com/en_us/kakute-v1-0.html?___store=en_us. [Accessed: 31- Jan- 2018].

[18] "HKPilot32 Autonomous Vehicle 32Bit Control Set w/ Power Module", Hobbyking. [Online]. Available: https://hobbyking.com/en_us/hkpilot32-

autonomous-vehicle-32bit-control-set-w-power-module.html?___store=en_us. [Accessed: 31- Jan- 2018].

[19] "Px4Pilot 32Bit AutoPilot Flight Controller", Hobbyking. [Online]. Available: https://hobbyking.com/en_us/px4pilot-32bit-autopilot-flight-controller.html?___store=en_us. [Accessed: 31- Jan- 2018].

[20] "TauLabs Sparky 2.0 32bit Flight Controller", Hobbyking. [Online]. Available: https://hobbyking.com/en_us/taulabs-sparky-2-0-32bit-flight-controller.html?___store=en_us. [Accessed: 31- Jan- 2018].

[21] "Introducing the AUAV X2.1 Flight Controller", Diydrones.com. [Online]. Available: https://diydrones.com/profiles/blogs/introducing-the-auav-x2-1-flight-controller. [Accessed: 06- Feb- 2018].

[22] D. Vissière, F. Callou, N. Petit, and P .Bristeau, “The Navigation and Control Technology Inside the AR.Drone Micro UAV”, Centre Automatique et Systèmes, Unité Mathématiques et Systèmes, Paris, France, 2011.

[23] "RE1 Flight Controller - BrainFPV", brainfpv. [Online]. Available: https://www.brainfpv.com/re1/. [Accessed: 16- Feb- 2018].

[24] KISS FC 32bit Flight Controller V1.03", Fpvmodel.com. [Online]. Available: https://www.fpvmodel.com/kiss-fc-32bit-flight-controller-v1-03_g1214.html?u=C752F9166E3E92BD. [Accessed: 16- Feb- 2018].

[25] "BetaflightF4 Flight Controller", Fpvmodel.com. [Online]. Available: https://www.fpvmodel.com/betaflightf4-flight-controller_g1351.html?u=C752F9166E3E92BD. [Accessed: 16- Feb- 2018].

[26] "Matek Systems BetaFlight F405-AIO", www.banggood.com. [Online]. Available: https://www.banggood.com/Matek-Systems-BetaFlight-F405-AIO-STM32F405-Flight-Controller-Built-in-PDB-5V2A-9V2A-Dual-BEC-p-1165338.html?p=Y810093989372201603X&cur_warehouse=CN. [Accessed: 16- Feb- 2018].

[27] "DYS F4 Flight Controller", Fpvmodel.com. [Online]. Available: https://www.fpvmodel.com/dys-f4-flight-controller_g1268.html?u=C752F9166E3E92BD. [Accessed: 16- Feb- 2018].

[28] R. Garbacz and E. Newman, “Characteristic modes of a symmetric wire cross,” IEEE Trans. Antennas Propag., vol. 28, no. 5, pp. 712–715, Sep. 1980.

[29] A. M. Hassan, F. Vargas-Lara, J. F. Douglas, and E. J. Garboczi, “Electromagnetic Resonances of Individual Single-Walled Carbon Nanotubes With Realistic Shapes: A Characteristic Modes Approach,” IEEE Trans. Antennas Propag., vol. 64, no. 7, pp. 2743–2757, Jul. 2016.

5) Focus Wave Mode (FWM)

Here we report a summary of the launch and propagation of electromagnetic short pulse from a uniformly excited circular aperture. This study is based on earlier investigations by other researchers and summarizes the results of a literature search and our current progress. Preliminary results suggest that EM pulses with smaller rise times can

effectively launch electromagnetic waves whose time-average Poynting power density exhibits minimal spatial decay compared to the corresponding time-harmonic (steady-state) excitation. A low-profile, ultra-wideband micro-strip patch antenna was designed and simulated to demonstrate its potential feasibility of launching minimally dispersive short EM pulses. In addition, a brief comparative analysis of launching Bessel beams is included. Further investigations into EM pulse propagation and design of UWB antennas is suggested. The results demonstrate the feasibility of application of short EM pulses for C-sUAV scenarios relevant to the project.

A. Introduction

Non-destructive disabling of the functionalities of remotely-located hostile mobile units, gainful utilization of RF propagation mechanisms appear to be a judicious choice. This choice can be effected if the conventional spatial decay of the power density, *i.e.*, the $\frac{1}{r^2}$ loss, where *r* is the distance, can be reduced. If this is made feasible, then one can launch electromagnetic waves with much higher power density, implying large amounts of power impinging on communication devices located within the hostile units. To that end, the subject of this investigation is to explore possibilities for launching EM waves that have minimal spatial dispersion.

The concept of EM missiles [1], [2] and Focus Wave Modes (FWM) [3]-[5] explored this aspect and concluded that pulsed excitations can launch EM waves with *minimal* dispersion. However, FWM requires an infinite aperture to essentially launch plane waves that have no spatial decay. It was argued in [5] that FWM have little practical utility. In contrast, EM missiles decay slowly and experimental confirmation [2] suggests it as a strong candidate for launching minimally dispersive waves. Other non-diffracting waves like Bessel, Gauss, Airy and Laguerre beams have been reported [6],[7] but are of little use to the present effort because the results were restricted mostly to optical frequencies. In addition, the analysis primarily revolves around the use of Fourier-Bessel series to develop scalar potentials [6, p. 45, Eq. (27)], with its attendant approximations, but there is no direct result available to compute power density decay. More importantly, since the solutions were developed based on homogeneous wave equations, it did not appear to be directly the source (antenna) that would launch such non-dispersive waves. The main purpose of this investigation was to understand mechanisms of practical antenna topologies at microwave frequencies that can launch such minimally dispersive waves.

A review of [1], [2], [8], [9] suggested that it is possible to launch “electromagnetic missiles” provided suitable pulsed excitations are realized. It was fortuitous that the time-average Poynting vector [8, Eq. (14)], [9, Eq. (71)] was available and was related to a specific antenna excitation. The results presented in this report are from [8] because the corresponding formulations in [9] are numerically difficult to implement and are currently under investigation.

The primary limitations of the results in [8] and [9] are enumerated as below:

- In [8] the Poynting power density appears to be accurate for the high-frequency part of the spectrum of the pulse excitation. In [9] the pulse spectrum has been assumed as $\mathcal{O}\left(\frac{1}{\omega^{\frac{1}{2}}}\right)$ without any specific reference to any form of pulse excitation.

- The result in [8] is valid beyond the Rayleigh distance. Thus, it is not known how the strength of the Poynting power density varies at distances smaller than the Rayleigh range. Fundamental understanding of this limitation is necessary to develop a launching mechanism of minimal dispersive waves at arbitrary distances. Similar remarks apply to [9].

- In both [8] and [9] the Poynting power density results are valid for on-axis (boresight) propagation. Thus, unlike phased arrays, one cannot steer the minimally dispersive beams off-axis.

It may be argued that the first and third bullet points above are somewhat serious limitations in gainfully exploiting the features of minimally dispersive, short-pulse electromagnetic waves.

In what follows, the formulation from [8] are briefly summarized next. Relevant formulas for Bessel beam generation from [14] are included. This is followed by results from [8] and [14] for the spatial decay of the Poynting vector and electric field intensity, respectively. Results for pulse rise times and required bandwidths are also included. The launch of minimally dispersive requires design of ultrawideband antennas [10]-[13]. To that end, a possible UWB antenna is designed based on the information from [15], and its potential applicability for minimally dispersive waves (MDW) is discussed.

The report closes by outlining the scope for future work, and is followed by a selected list of references.

B. Analysis of EM Pulse Propagation

The EM pulse propagation from a spatially-uniform, pulse excited circular aperture has been rigorously analyzed by employing the space-time, causal Green's function in [8]. The Fourier transform has been utilized and the electric and magnetic fields have been obtained, which then has been subsequently used in determining the time-averaged Poynting vector. Note that the Poynting vector finally depends, after the time average operation, on the constant pulse parameters. Finally, the scalar component of the Poynting vector normal to the aperture is determined. Relevant results for pulsed and time-harmonic excitations are summarized below from [8] and [11, pp. 385-388], respectively for the geometry in Figure 39.

C. Pulsed Excitation

The externally impressed source current (magnetic type for aperture) is given by:

$$\vec{\mathbf{J}}_{\mathbf{i}} = \hat{\boldsymbol{x}} f(t)\delta(z) \;\ldots\ldots\;\; (1)$$

The sinusoidally modulated time signal in (1) is given by

$$f(t) = \mathrm{I}_0 \left(\frac{t}{\mathrm{T}}\right)^{2\nu-1} e^{\frac{-t}{\tau}} \sin(\Omega_c t)\mathrm{H}(t) \;\ldots..\; (2)$$

In (2) I_0 is the current amplitude for the temporal part; ν is the pulse rise time coefficient; T is a constant in time units (secs); τ characterizes the eventual pulse falloff; $\Omega_c = 2\pi f_c$ is the radian frequency corresponding to the modulating sinusoidal frequency, and, $\mathrm{H}(t)$ is the standard unit step function.

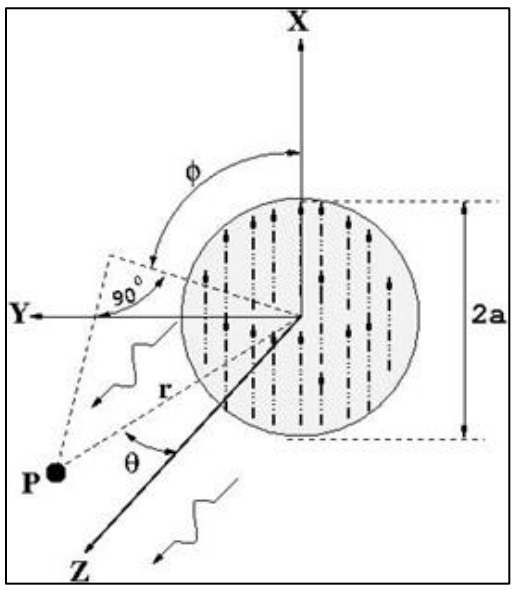

Figure 39. *Geometrical details of a circular aperture excited by a pulse in the x-y plane. The time-average Poynting vector (power flux) along the z-direction is of interest for this.*

Upon determining the electric $\vec{\mathbf{E}}$ and magnetic flux $\vec{\mathbf{B}}$ densities via the free-space Green's function method, the time-average (scalar) Poynting vector is determined through the relationship

$$U(z) = \frac{c}{4\pi}\int_{-\infty}^{+\infty} dt\{\hat{\mathbf{z}} \cdot (\vec{\mathbf{E}} \times \vec{\mathbf{B}})\} \;\;\ldots.\;\; (3)$$

Evaluation of (3) utilizes the Fourier transform of (2) that is given by the result

$$\tilde{f}(\omega) = j\mathrm{I}_0 \frac{\Gamma(2\nu)}{2\mathrm{T}^{2\nu-1}}\left[\left(\frac{1}{\tau} - j(\omega - \Omega_c)\right)^{-2\nu} - \left(\frac{1}{\tau} - j(\omega + \Omega_c)\right)^{-2\nu}\right] \;\ldots..\; (4)$$

In (4), the Fourier transform is evaluated for $-\infty \leq \omega \leq +\infty$; $\Gamma(z)$ is the standard gamma function. The final expression for the Poynting power density, that has been further specialized in the far field ($z \to \infty$), making use of (3), is given by the result

$$U(z) \approx \frac{2\sqrt{\pi}\mathrm{I}_0{}^2\mathrm{T}(\Omega_c\mathrm{T})^2}{c}\left[\frac{\Gamma(1+2\nu)\Gamma\left(\frac{1}{2}-2\nu\right)}{1+4\nu}\right]\left(\frac{\mathrm{d}^2}{4c\mathrm{T}z}\right)^{1+4\nu} \text{.....(5)}$$

It is shown in [8] that (5) is valid whenever $|\nu| < \frac{1}{4}$, or, $\frac{-1}{4} < \nu < \frac{+1}{4}$. In (5) $d = 2a$ is the diameter of the circular aperture, as in Fig. 1. The time-harmonic excitation is discussed next.

D. Time Harmonic Excitation

For the same geometry in Figure 39, and for a constant spatial excitation, the far-zone electric field at any point outside the aperture is given by [11, p. 386]:

$$\vec{\mathbf{E}} = \left(\hat{\boldsymbol{\theta}}\cos\phi - \hat{\boldsymbol{\phi}}\sin\phi\cos\theta\right)\frac{E_0\pi a^2 j\beta}{2\pi r}e^{-j\beta r}\left[\frac{J_1(\beta a\sin\theta)}{(\beta a\sin\theta)}\right] \text{ ..... (6)}$$

The Poynting power density along the z-axis can be calculated easily by specializing the above for$\theta = 0^o$. This final result is given by

$$V(z) = \frac{1}{\eta_0}\left(\frac{E_0\pi a^2}{\lambda}\right)^2\frac{1}{z^2} \text{ ..... (7)}$$

Thus, in the final comparisons we need to use (5) and (7) for examining the spatial decay of Poynting power density. There is one important observation. The units of (7) are in Watts/m^2 ; whereas the units of (5) are not so clearly defined. Therefore, only a relative comparison can be done for understanding the nature of spatial decay. The results for the Bessel beam are included next from [14].

E. Time-Harmonic Bessel Beams

Bessel beams are launched by leaky waves [14]. The excitation of leaky waves by a circular cavity is investigated in [14]. The geometry is shown in Figure 40.

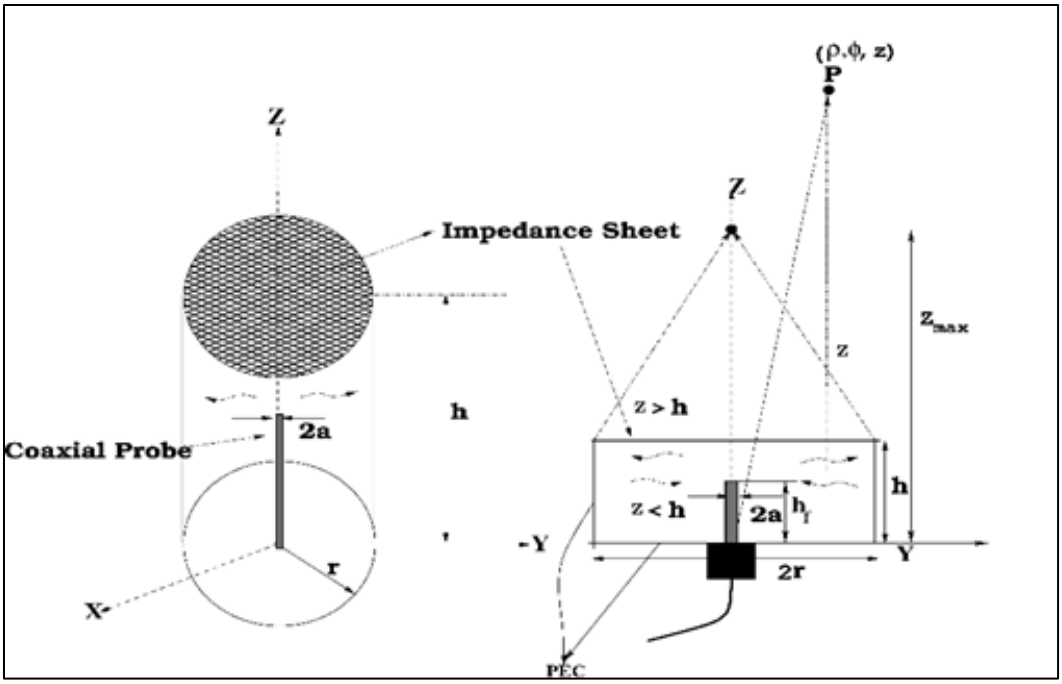

***Figure 40**. A coaxial probe-fed circular cavity covered by an impedance sheet. The surface impedance generates the leaky waves in form of Bessel beams by use of the equivalence principle.*

The ρ- and z- components of the electric fields outside the aperture are given by:

$$E_z = C_0 \left[\begin{array}{c} \rho \int_0^a x J_1(k_\rho x) dx \int_0^{2\pi} d\varphi \left\{ \frac{e^{-jkR}}{R^3} (1 + jkR) \right\} - \int_0^a x^2 J_1(k_\rho x) dx \\ \times \int_0^{2\pi} d\varphi \left\{ \frac{e^{-jkR}}{R^3} (1 + jkR) \cos(\phi - \varphi) \right\} \end{array} \right]$$

..... (8)

for the z-component, and

$$E_\rho = -C_0 (z - h) \int_0^a x\, J_1(k_\rho x) dx \int_0^{2\pi} d\varphi \left\{ \frac{e^{-jkR}}{R^3} (1 + jkR) \right\}$$

..... (9)

for the ρ-component. The distance from the center of the aperture the observation point P is given by:

$$R = \sqrt{\rho^2 + x^2 - 2\rho x \cos(\phi - \varphi) + (z - h)^2}$$ ..... (10)

F. Results and Discussions

The results are shown for the comparison of the Poynting power density and the spatial decay of the electric field for Bessel beams. In addition, the bandwidth characteristics of a UWB antenna is included.

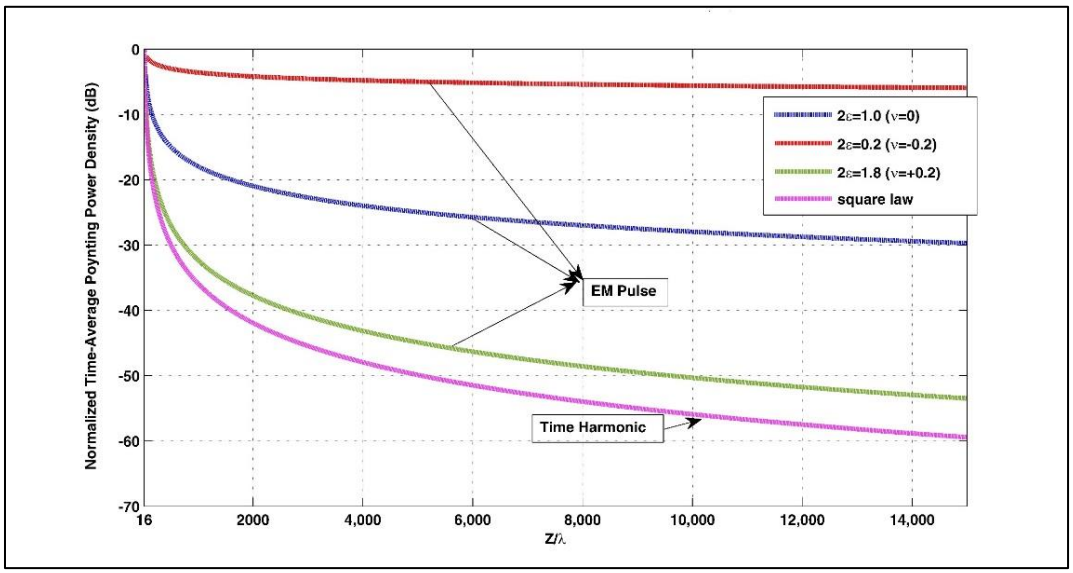

Figure 41. *Results for the spatial decay of Poynting power density from (5) and (7). The smaller values of the pulse rise index v exhibit much slower decay of power density. The data was generated for a frequency of 1 GHz. The 16λ distance is the Rayleigh range.*

The result in Figure 41 shows that at about $14{,}000\lambda \cong 4$ Km (at 1GHz) the difference of about 50 dB exists between pulse and time-harmonic excitations. To generate a pulse corresponding to $\nu = -0.2$ in Figure 42 several pulse waveforms were considered and the rise time was determined. The pulse signal is given by (2) above. The results are shown below in Figure 42. The rise time for the pulse corresponding to $\nu = -0.2$ in Figure 42 was determined manually and it turned out to be $t_r \cong 70 \times 10^{-12}$ seconds. This corresponds to a bandwidth that is calculated by the formula [12]

$$t_r = \frac{0.35}{BW} \text{..... (11)}$$

This gives a bandwidth of 5 GHz. Next, to understand if indeed such a bandwidth can be obtained, a UWB design was conceived from the information in [15]. The antenna geometry and the corresponding important result for the VSWR are shown. The bandwidth was considered for the 2:1 VSWR range or -10 dB return loss. Figure 43 shows the type of micro-strip antenna that was designed and simulated.

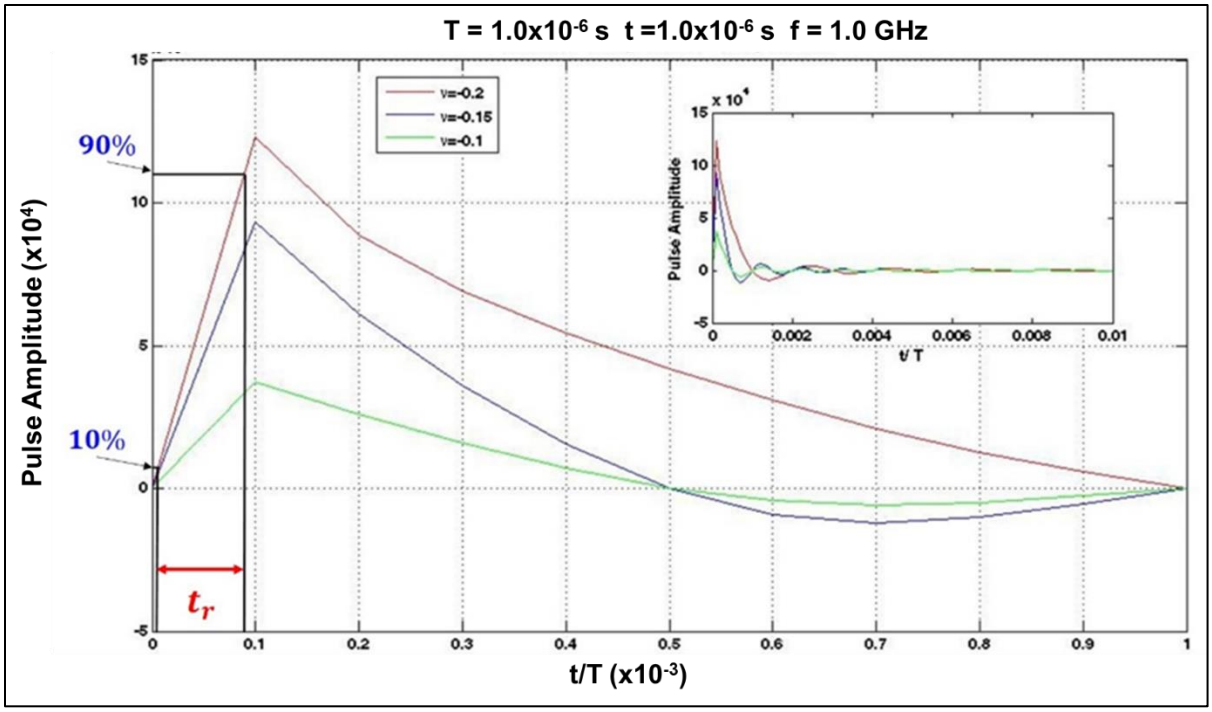

Figure 42. *Calculation of the pulse rise times for various pulse rise indices. This refers to equation (2) here in the report.*

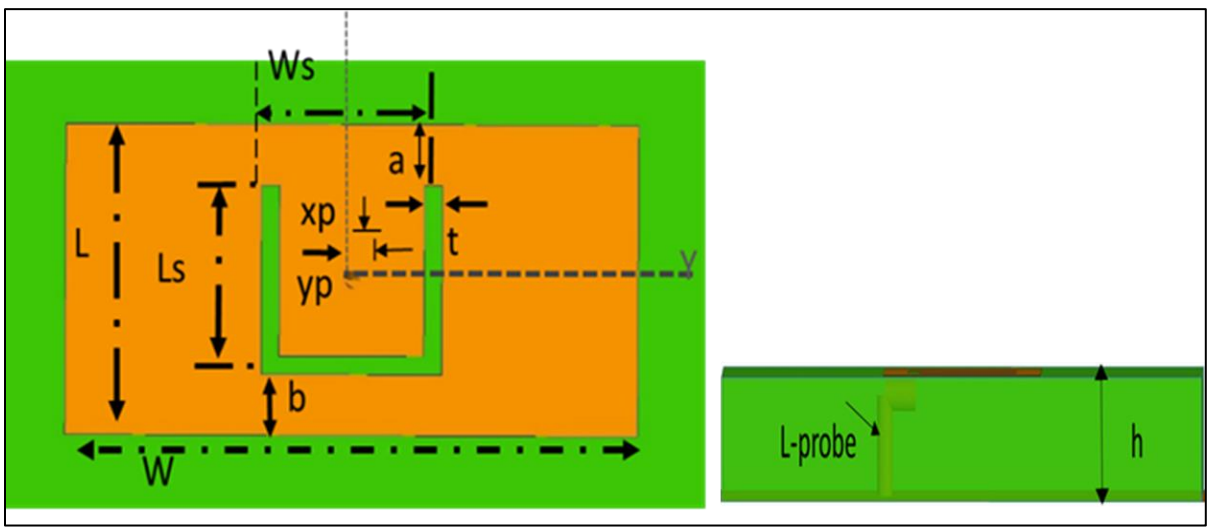

Figure 43. *Proximity coupled L-Probe fed U-Slot microstrip patch antenna. The typically important dimensions are: h=5.09, ε_r=3.27, W=28.48, L=13.4, L_s=9.66, W_s=9.63, t=1.00, b=2.08, x_p=0, y_p=0. All dimensions in mm.*

The corresponding VSWR and boresight gain for the antenna in Figure 44 are shown below.

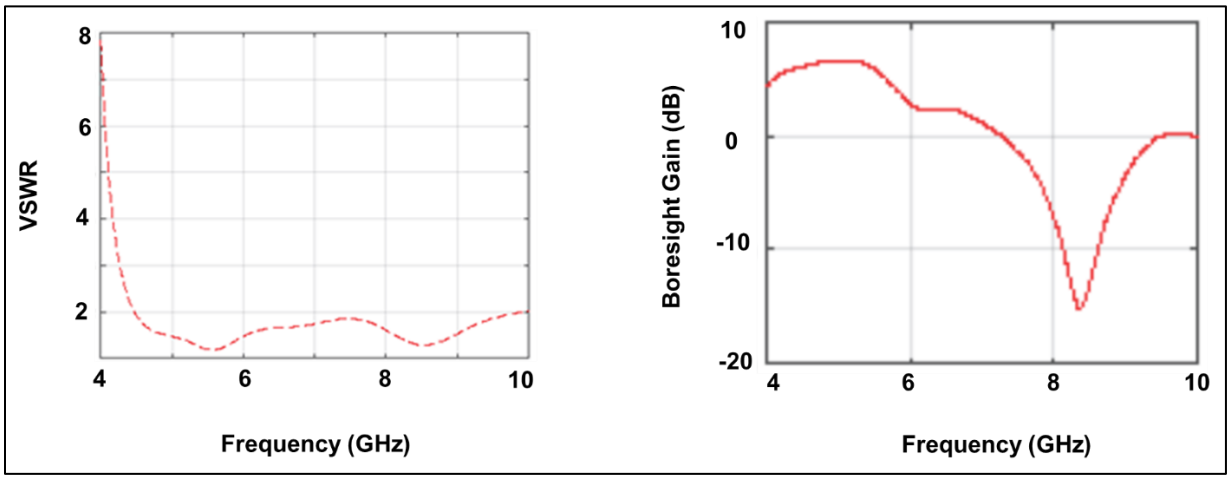

Figure 44. *VSWR and Gain results for the Proximity-coupled L-Probe fed U-Slot microstrip patch antenna in Fig. 5. The -10 dB return loss bandwidth is from 4.5 GHz to 10 GHz (or 5.5 GHz). This bandwidth can generate a pulse with a rise time of 63.6×10^(-12) sec.*

The result for the spatial decay of electric fields from a Bessel beam are shown in Figure 45.

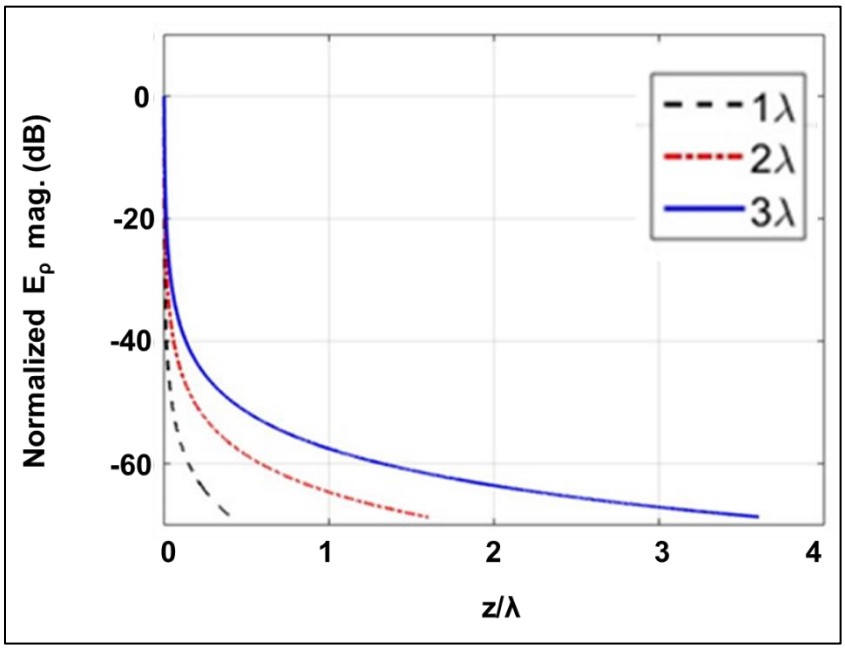

Figure 45. *Spatial decay of Eρ, equation (9), along the z-axis for the cavity shown in Figure 40, for various cavity radii at 1 GHz.*

The results in Figure 45 shows that larger radii have a slower decay. This is because the “diffractive” distance given by [14, Eq. (24)], reads:

$$Z_{max} = a\sqrt{\left(\frac{k_0}{\beta_\rho}\right)^2 - 1} \text{..... (12)}$$

which linearly increases with the cavity radius *a*. However, the nature of decay suggests that it may not be useful for larger distances. In (12) β_ρ is the propagation constant of the leaky wave, and, k_0 is the free-space propagation constant.

The information gleaned from the above results suggests that:

1) The short pulse can launch minimally dispersive EM waves that are stronger than time-harmonic fields.
2) Ultrawideband antennas with a defined signal spectrum can launch such short pulse EM waves.
3) Bessel beams are not recommended for long range applications.

G. Future Investigation

The following are recommended for future investigations:

1) Improved analysis of UWB antennas that are consistent with the Harrington and Gustafsson limits [13].
2) Comprehensive analysis of short EM pulse radiation that considers the complete spectrum, and, off-boresight launch directions.
3) Explore other types of UWB antennas, such as the microstrip patch, that can launch minimally dispersive waves.
4) Experimental characterization of EM pulse propagation (minimally dispersive waves) using UWB antennas.

H. Summary and Conclusions

This preliminary investigation explored the possibility of launching minimally dispersive waves. It was found from the state-of-art information that suitably designed short pulses can launch EM waves with minimal spatial decay. The use of ultrawideband antennas was investigated with promising results. Further research issues have been identified, based on the results, for the future.

I. References

[1] T. T. Wu, “Electromagnetic Missiles,” *Journal of Applied Physics*, vol. 57, no. 7, pp. 2370-2373, April 1985.

[2] H.-M. Shen and T. T. Wu, “The Properties of the Electromagnetic Missiles,” *Journal of Applied Physics*, vol. 66, no. 9, pp. 4025-4034, November 1989.

[3] J. N. Brittingham, "Focus Wave Modes in Homogeneous Maxwell's Equations: Transverse Electric Mode," *Journal of Applied Physics*, vol. 54, no. 3, pp. 1179-1189, March 1983.

[4] R. W. Ziolkowski, "Exact Solutions of the Wave Equation with Complex Source Locations," *Journal of Mathematical Physics*, vol. 26, no. 4, pp. 861-863, March 1983.

[5] E. Heyman, B. Z. Steinberg and L. B. Felsen, "Spectral Analysis of Focus Wave Modes," *Journal of the Optical Society of America* A, vol. 4, no. 11, pp. 2081-2091, November 1987.

[6] H. E. Hernandez-Figueroa, M. Zamboni-Rached and E. Recami (eds.), *Localized Waves*. John-Wiley & Sons, Inc., 2008, NJ, USA.

[7] H. E. Hernandez-Figueroa, E. Recami and M. Zamboni-Rached (eds.), *Non-Diffracting Waves*. Wiley-VCH, Weinheim, Germany, 2008.

[8] B. Hafizi, "Effects of Carrier and Dispersion on Propagation of a Directed Electromagnetic Pulse," *Journal of Applied Physics*, vol. 73, no. 2, pp. 513-521, January 1993.

[9] T. T. Wu and H.-M. Shen, "Radiation of an Electromagnetic Pulse from the Open End of a Circular Waveguide," *SPIE Proceedings*, vol. 873, *Microwave and Particle Beam Sources & Propagation*, pp. 329-337, 1988.

[10] T. B. Hansen and A. D. Yaghjian, *Plane-Wave Theory of Time-Domain Fields: Near-Field Scanning Applications*. NY, USA: IEEE Press, 1999.

[11] W. L. Stutzman and G. A. Thiele, *Antenna Theory and Design* (3rd edition). John-Wiley & Sons, Inc., 2013, NJ, USA.

[12] Hans. G. Schantz, *The Art and Science of Ultrawideband Antennas* (2nd edition). Boston, MA, USA: Artech-House, 2015.

[13] J. L. Volakis, C.-C. Chen and K. Fujimoto, *Small Antennas: Miniaturization Techniques and Applications*. NY, USA: McGraw-Hill, 2010.

[14] M. Ettore and T. Grbic, "Generation of Propagating Bessel Beams using Leaky-Wave Modes," *IEEE Transactions on Antennas and Propagation*, vol. 60, no. 8, pp. 3606-3613, August 2012.

[15] M. Khan and D. Chatterjee, "Characteristic Mode Analysis of a Class of Empirical Design Techniques for Probe-fed, U-Slot Microstrip Patch Antennas," *IEEE Transactions on Antennas and Propagation*, vol. 64, no. 7, pp. 2758-2770, July 2016.

Appendix

Monthly Status Reports

SECTION REMOVED

See ***ONR Short Pulse Research, Evaluation and non-SWaP Demonstration for C-sUAV Study:*** *Annual Report Appendix 2018*